JCB Journal of Cell Biology

ARTICLE

Excitable RhoA dynamics drive pulsed contractions in the early *C. elegans* embryo

Jonathan B. Michaux[1]*, François B. Robin[1]*, William M. McFadden[2], and Edwin M. Munro[1,3]

Pulsed actomyosin contractility underlies diverse modes of tissue morphogenesis, but the underlying mechanisms remain poorly understood. Here, we combined quantitative imaging with genetic perturbations to identify a core mechanism for pulsed contractility in early *Caenorhabditis elegans* embryos. We show that pulsed accumulation of actomyosin is governed by local control of assembly and disassembly downstream of RhoA. Pulsed activation and inactivation of RhoA precede, respectively, the accumulation and disappearance of actomyosin and persist in the absence of Myosin II. We find that fast (likely indirect) autoactivation of RhoA drives pulse initiation, while delayed, F-actin–dependent accumulation of the RhoA GTPase-activating proteins RGA-3/4 provides negative feedback to terminate each pulse. A mathematical model, constrained by our data, suggests that this combination of feedbacks is tuned to generate locally excitable RhoA dynamics. We propose that excitable RhoA dynamics are a common driver for pulsed contractility that can be tuned or coupled differently to actomyosin dynamics to produce a diversity of morphogenetic outcomes.

Introduction

Pulsed contractility is a widespread mode of actomyosin contractility expressed by many non-muscle cells in which transient accumulations of F-actin and Myosin II accompany local contractions of the cell surface. Pulsed contractions were first identified in the polarizing *Caenorhabditis elegans* zygote (Munro et al., 2004) and have now been documented in a wide variety of embryonic and extra-embryonic epithelia (Martin et al., 2009; Solon et al., 2009; Blanchard et al., 2010; David et al., 2010; He et al., 2010; Rauzi et al., 2010) and mesenchymal cells (Kim and Davidson, 2011). A similar phenomenon, known as cell shape oscillations, has been observed in many cultured cells (Salbreux et al., 2007; Kapustina et al., 2008; Sedzinski et al., 2011). Pulsed contractions produce transient shape changes that can be biased or rectified in different ways to produce distinct morphogenetic outcomes, such as tissue invagination (Martin et al., 2009), tissue elongation (He et al., 2010; Rauzi et al., 2010; Levayer and Lecuit, 2013), epithelial tissue closure (Solon et al., 2009), and wound healing (Razzell et al., 2014). During embryonic development, pulsed contractions may represent an adaptation to accommodate rapid cell and tissue deformations while maintaining overall tissue integrity (Vasquez et al., 2014). In other contexts, such as in many cultured cells, shape oscillations may represent an aberrant behavior that manifests when cells lose normal adhesion to their substrates (Paluch et al., 2005; Salbreux et al., 2007), when microtubules are depolymerized (Bornens et al., 1989; Werner et al., 2007; Kapustina et al., 2008, 2013; Piekny and Glotzer, 2008; Rankin and Wordeman, 2010), or when contractile tension is very high during cytokinesis (Sedzinski et al., 2011).

Despite the widespread occurrence of pulsed contractions and increasing evidence for their functional relevance, the mechanisms that initiate and terminate pulsed contractions remain poorly understood. From a dynamic perspective, pulsed contractions represent a form of excitable behavior, exemplified by action potentials in neuronal cells (Izhikevich, 2007) or pulses of intracellular calcium release observed in many cell types (Goldbeter, 1996). Theoretical studies highlight two key ingredients for excitability: positive feedback to drive a rapid upswing in activity and delayed negative feedback to bring it back down again. A key challenge is to identify the specific modes of positive and negative feedback that drive pulsed contractions.

Multiple forms of positive feedback could contribute to initiating pulsed contractions. For example, local actomyosin-based contraction could promote further accumulation of actomyosin through mechanosensitive motor-filament binding (Effler et al., 2006; Fernandez-Gonzalez et al., 2009; Ren et al., 2009; He et al., 2010; Schiffhauer et al., 2016), by enhancing actin filament

---

[1]Department of Molecular Genetics and Cell Biology, University of Chicago, Chicago, IL; [2]Biophysics Program, University of Chicago, Chicago, IL; [3]Institute for Biophysical Dynamics, University of Chicago, Chicago, IL.

*J.B. Michaux and F.B. Robin contributed equally to this paper; Correspondence to François B. Robin: francois.robin@upmc.fr; Edwin M. Munro: emunro@uchicago.edu; F.B. Robin's present address is Sorbonne Universités, University Pierre and Marie Curie Paris 06, Centre National de la Recherche Scientifique, Institut National de la Santé et de la Recherche Médicale, Biologie du Développement Paris Seine—Institut de Biologie Paris Seine, Paris, France.

Rockefeller University Press
J. Cell Biol. 2018 Vol. 217 No. 12 4230–4252

https://doi.org/10.1083/jcb.201806161

assembly and/or stability (Hayakawa et al., 2011; De La Cruz and Gardel, 2015) or by transporting and concentrating actomyosin and/or its upstream activators (White and Borisy, 1983; Dierkes et al., 2014; Munjal et al., 2015). Alternatively, dynamic clustering of F-actin and/or Myosin II by scaffolding proteins such as Anillin could promote Myosin II recruitment and focal contraction (Maddox et al., 2005). Finally, autocatalytic activation of upstream regulators such as RhoA could drive local excitation independent of, or in addition to, myosin-based tension or network contraction (Bement et al., 2015; Munjal et al., 2015; Zhang and Glotzer, 2015; Graessl et al., 2017). Similarly, multiple forms of delayed negative feedback could contribute to terminating pulses, including progressive buildup of steric or elastic resistance to further contraction (Dierkes et al., 2014), contraction-mediated disassembly, or delayed recruitment of disassembly factors or inhibitors of Myosin II or RhoA (Kasza and Zallen, 2011; Bement et al., 2015; Munjal et al., 2015; Graessl et al., 2017).

Here, we combined quantitative imaging with experimental manipulations and mathematical modeling to identify the dynamic basis for pulsed contractility in the early *C. elegans* embryo. Using single-molecule imaging and particle-tracking analysis, we provide definite evidence that the initiation of pulsed contractions does not involve or require local redistribution of actomyosin or its upstream activators. Instead, pulsed contractions are driven by local pulses of RhoA activity, which feed forward to control local accumulation of downstream targets F-actin, Myosin II, and Anillin. We present evidence that pulsed accumulation of RhoA is governed by locally excitable RhoA dynamics: Local autocatalytic activation of RhoA drives the rapid upswing of RhoA activity during pulse initiation, while F-actin–dependent recruitment of the redundantly acting RhoA GTPase-activating proteins (GAPs) RGA-3/4 provide delayed negative feedback to terminate the pulse. A minimal model, sharply constrained by our experimental data, suggests that this combination of feedbacks is sufficient to generate locally excitable or oscillatory RhoA dynamics and to explain quantitatively the temporal dynamics of RhoA activation and RGA-3/4 accumulation during each pulse. We propose that excitable RhoA dynamics define a core mechanism for pulsed contractility and suggest that this mechanism may be tuned or filtered through downstream effectors to control the size or spacing or lifetime of pulsed contractions.

Results

Pulsed contractions were originally described in *C. elegans* during interphase in the polarizing one-cell zygote (P0; Fig. 1, A–C [individual pulses indicated by white arrowheads in Fig. 1 B]; and Video 1, top; Munro et al., 2004). In these cells, pulsed contractions are associated with transient deep invaginations of the cell surface (Fig. 1, A and B, magenta arrows); this makes it more difficult to quantify local changes in the density of cortical factors during individual pulses because these measurements could be confounded by movements of the cortex in and/or out of the plane of focus. Therefore, we focused on pulsed contractions that occur at the two-cell stage in the anterior blastomere (AB; Fig. 1, D–F [individual pulses indicated by white arrowheads in Fig. 1 E]). As in P0, pulsed contractions in the AB involve transient accumulations of F-actin and Myosin II; they are associated with transient local contractions of the actomyosin cortex (Fig. 1 F), but they are not associated with pronounced invaginations of the cell surface.

Single-molecule analysis of actomyosin dynamics during pulsed contractions

As a key step toward distinguishing different mechanisms for pulsed contractions, we used single-molecule imaging and single-particle–tracking analysis to quantify the relative contributions of local turnover and redistribution to changes in F-actin and Myosin II density during individual pulses. As described previously (Robin et al., 2014), we used RNAi against GFP to obtain embryos expressing single-molecule levels of Actin::GFP or of the non-muscle myosin heavy chain fused to GFP (NMY-2::GFP) over the endogenous proteins (Fig. 2 A and Videos 2 and 4). We combined near-total internal reflection fluorescence (TIRF) imaging with single-molecule detection and tracking to measure the appearance, motion, and disappearance of single-molecule speckles (Fig. 2, A–C; Robin et al., 2014). We assumed, as did others (Watanabe and Mitchison, 2002; Vallotton et al., 2004), that single-molecule appearance and disappearance events report directly on local rates of filament assembly and disassembly. We have shown previously that rates of turnover measured by single-molecule tracking agree well with those measured from single-molecule data by fitting kinetic models to photobleaching curves (Materials and methods; Robin et al., 2014).

We then devised new methods to measure simultaneously (a) single-molecule appearance rates, disappearance rates, and densities, and (b) local rates of cortical deformation on a moving and deforming patch of cortex during individual pulsed contractions (Fig. S1; see Materials and methods for details). In brief, we identified a reference frame for each pulse near the onset of contraction; within that frame, we identified a polygonal region of interest (ROI) containing the contracting patch (Fig. 2 A, dashed blue polygon, hereafter referred to as "the patch"). We propagated the patch forward and backward in time by extrapolating the displacements of tracked particles on or near its boundary (Fig. 2 D, Fig. S1, and Video 3). We then measured local deformation of the patch as frame-to-frame changes in patch area or by estimating a local strain rate from frame-to-frame displacements of the individual particles, with similar results in each case (Fig. 2 E and Fig. S2, A–C; Materials and methods). At the same time, we measured the number of molecules and single-molecule appearance and disappearance rates within the patch over time (Fig. 2, F–H). Finally, we aligned single-molecule measurements with respect to the onset or termination of individual contractions to produce a dynamic signature of actin assembly, disassembly, and deformation over the lifetime of a pulse (Fig. 3, A–D; and Fig. S2, D–F). These measurements allowed us to cleanly distinguish changes in single-molecule densities due to local assembly and disassembly from those due to local contraction (or expansion) of the cortical patch.

If pulses are initiated by positive feedback in which local contraction concentrates actomyosin and/or its upstream regulators, then the onset of actomyosin accumulation should coincide

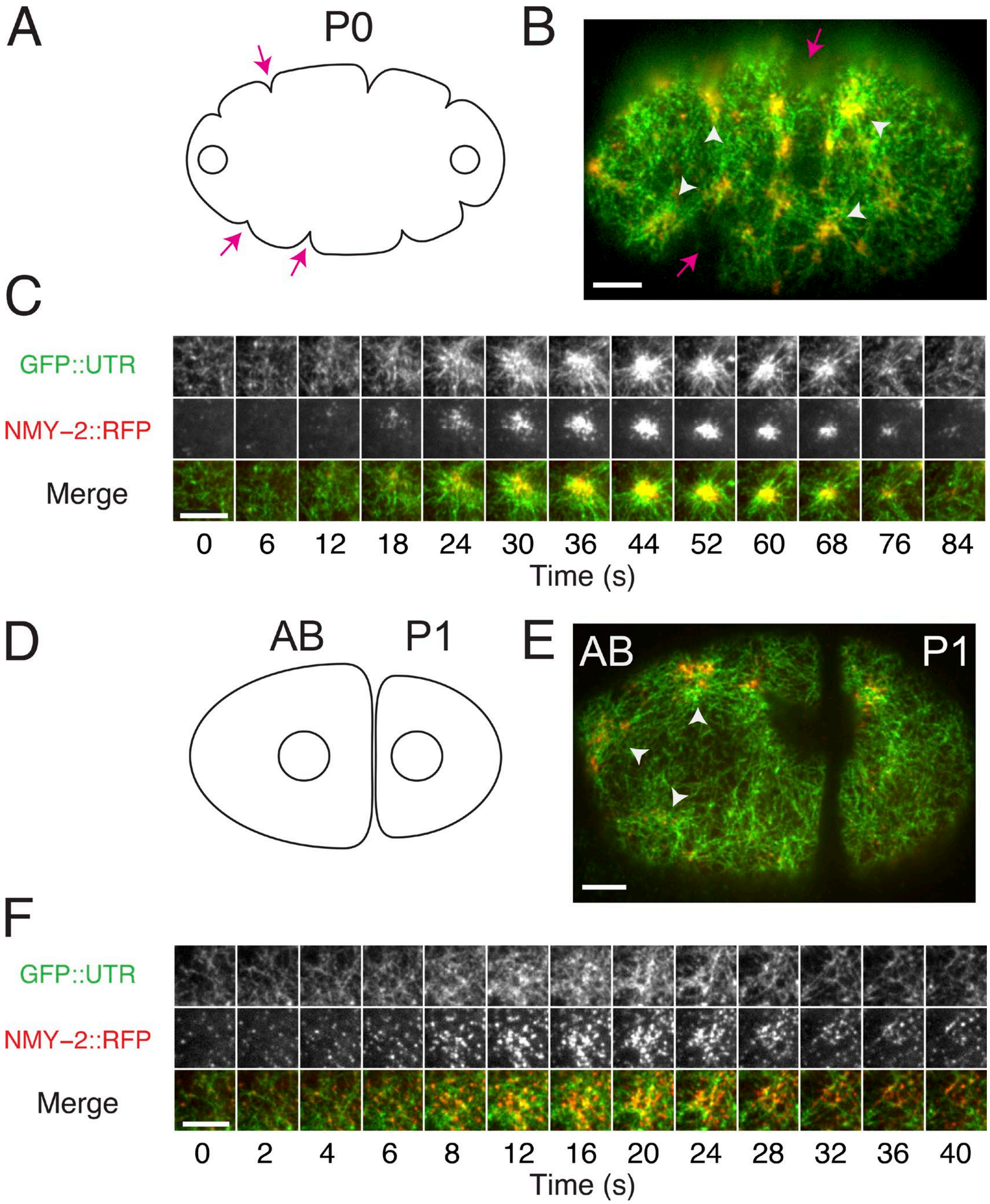

Figure 1. **Actomyosin pulses in one- and two-cell–stage embryos. (A)** Schematic view of the P0 during early interphase. Open circles represent the two pronuclei. **(B)** Micrograph of the P0 in early interphase expressing GFP::UTR and NMY-2::RFP. The white arrowheads (in B only) indicate individual pulses, and magenta arrows indicate membrane invaginations (ruffles). **(C)** Time evolution of a single pulse in the P0. The time delay between frames is 6 s for the first six frames and 8 s thereafter. **(D)** Schematic of an embryo at the early two-cell stage, showing the AB and the posterior blastomere P1. Open circles represent the interphase nuclei. **(E)** Micrograph of an early two-cell–stage embryo expressing GFP::UTR and NMY-2::RFP. White arrowheads indicate individual pulses. **(F)** Time evolution of a single pulse. The time delay between frames is 2 s for the first five frames and 4 s thereafter. Bars, 5 µm.

with the onset of contraction. Contradicting this expectation, we found that, on average, Actin:GFP began to accumulate ~5 s before the onset of contraction (Fig. 3, B and F; and Fig. S2, A–C), during a period of time in which the cortex was locally expanding (Fig. 3 A). Approximately 30% of the total increase in Actin::GFP single-molecule density measured during a pulse occurred before the onset of contraction (Fig. S2, A–C). This initial accumulation was entirely due to a net imbalance of assembly and disassembly (Fig. 3 E): Before the onset of contraction, assembly rates increased (Fig. 3 C) and disassembly rates decreased (Fig. 3 D), leading to a sharp increase in the net rate of single-molecule accumulation that peaked at the onset of contraction (Fig. 3 E). During the contraction phase itself, the rate of change in single-molecule densities was determined almost entirely by a net imbalance of assembly/disassembly, with a very minor (<6%) contribution from contraction itself (Fig. 3 E). Assembly rates

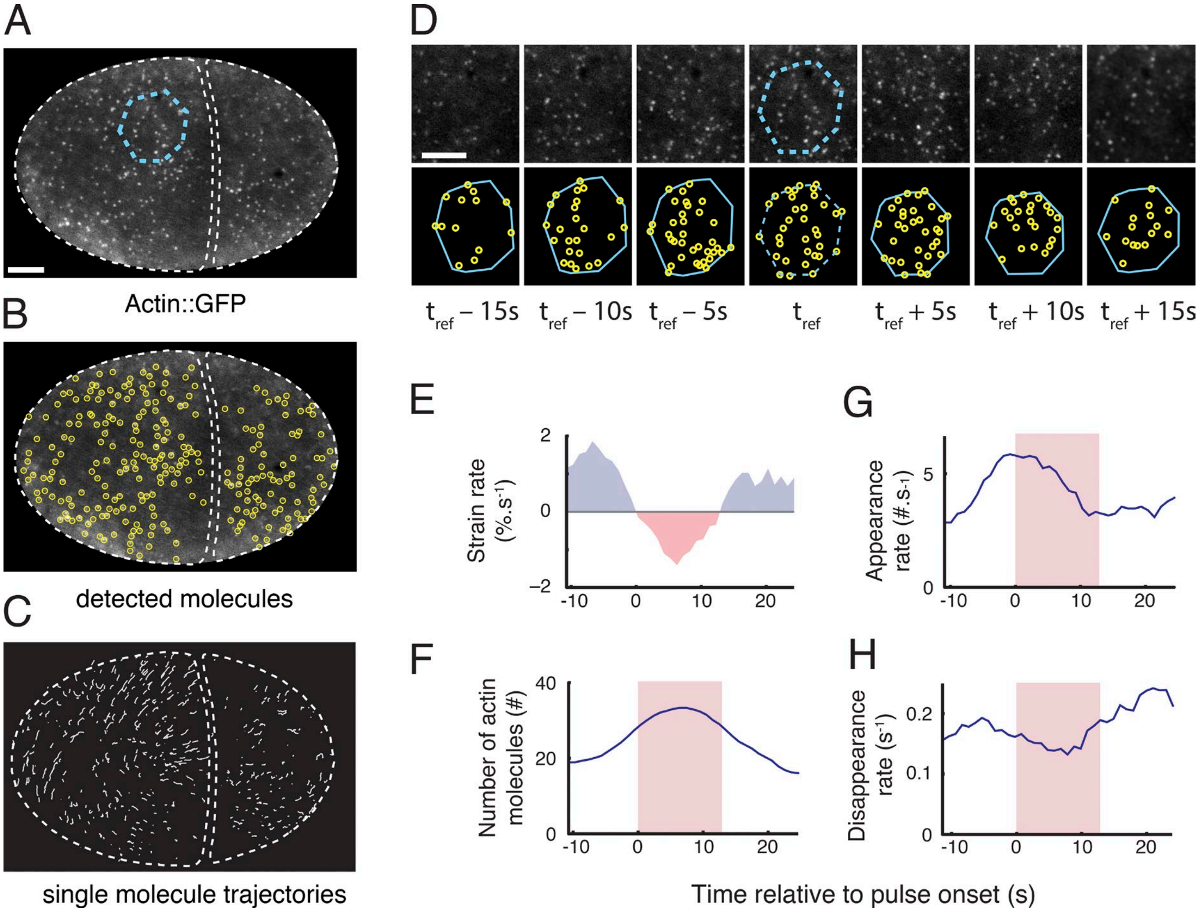

Figure 2. **Single-molecule analysis of actin network assembly, disassembly, and deformation during individual pulsed contractions. (A)** One frame of a time-lapse sequence taken from an embryo expressing low levels of Actin::GFP. A patch of cortex undergoing a pulse is identified from the time lapse sequence and outlined in cyan. **(B)** Automatic particle detection of single molecules from the image in A. **(C)** Trajectories of the molecules displayed in B that were tracked for longer than 2 s. **(D)** A polygonal ROI identified at time $t = t_{ref}$, in A (dashed cyan polygon) is propagated forward and backward in time by using the trajectories of tracked particles (see Materials and methods and Videos 2 and 3). **(E–H)** Simultaneous measurements of single-molecule dynamics and patch deformation over time. **(E)** Strain rate measured by using the particle-based method (see Materials and methods). **(F)** Number of actin molecules in the patch. Appearance rates (G) and disappearance rates (H) of actin molecules. Red shading in F–H indicates the time period in which the cortex is contracting locally (strain rate < 0). Bars: (A) 5 µm; (D) 3 µm.

decreased steadily, and disassembly rates increased steadily, such that a transition from net assembly to net disassembly (and from increasing density to decreasing density) occurred ~7 s after the onset of contraction (Fig. 3 E). We obtained very similar results in embryos depleted of ARX-2, an essential subunit of the ARP2/3 complex (Fig. S3), suggesting that our results are not strongly biased by selective incorporation of Actin::GFP into branched versus unbranched F-actin (Chen et al., 2012).

Single-molecule analysis of GFP-tagged Myosin II (NMY-2::GFP) revealed local assembly/disassembly dynamics that were strikingly similar to those measured for GFP::Actin. (Fig. 3, G–K). On average, the density of single molecules of NMY-2::GFP began to increase ~6 s before the onset of contraction during a period of local cortical expansion (Fig. 3 H), and ~50% of this increase occurred before the onset of contraction. As observed for GFP::Actin, the upswing in Myosin II before the onset of a contraction was associated with both a sharp increase in appearance rates and a sharp decrease in disappearance rates (Fig. 3, I and J); the net rate of increase peaked at the onset of contraction, and during the contraction phase, the rate of change in single-molecule densities was determined largely by a net imbalance of assembly/disassembly, with a minor contribution from contraction (Fig. 3 K).

In summary, we found that changes in the actomyosin density during pulsed contractions are governed primarily by a dynamic local imbalance of F-actin and Myosin II appearance and disappearance rates. A large fraction of the increase in F-actin and Myosin II density during each pulse occurs before the onset of contraction, and local contraction accounts for only a minor fraction of the subsequent density increase during the contraction phase itself. We conclude that changes in actomyosin density during pulsed contractions are governed primarily by dynamic modulation of assembly and disassembly, not by local clustering of these factors or by dynamic coupling of contraction and advection.

Pulsed activation of RhoA drives the pulsed accumulation of F-actin and Myosin II

The observation that F-actin and Myosin II accumulate with very similar kinetics during pulsed contractions suggests that their accumulation is driven by a common upstream regulator. An

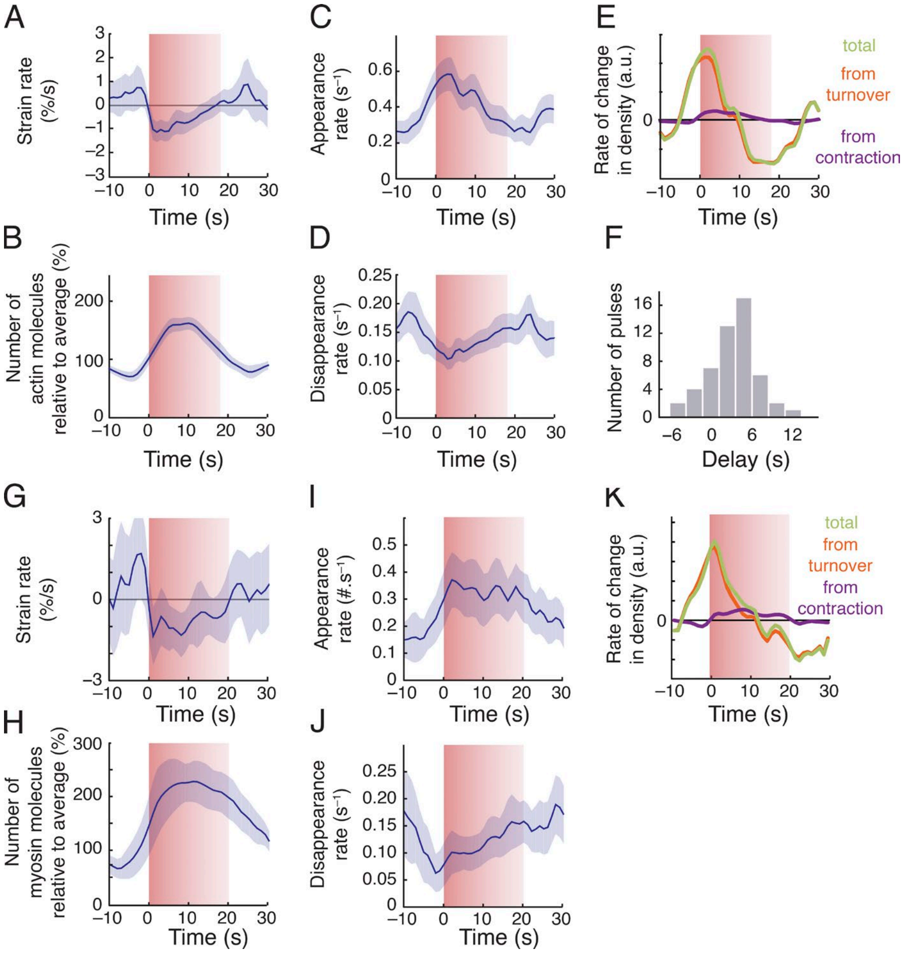

Figure 3. **Spatiotemporal modulation of assembly and disassembly drives transient accumulation of F-actin and Myosin II during pulsed contractions. (A–D)** Data from individual pulses, aligned with respect to the onset of contraction and then averaged to display particle-based strain rate (A), numbers of actin molecules (scaled by the average number for each pulse; B), appearance rate (C), and disappearance rate (D) versus time. **(E)** Total rate of change in actin density (green) and the individual contributions to rate of change from turnover (red) and surface contraction (purple). **(F)** Distribution of time delays between the initiation of contraction and actin accumulation. Data in A–F were averaged over 42 pulses, collected in eight embryos. **(G–J)** Average myosin dynamics synchronized with respect to time at which myosin density reached peak levels during a pulse, displaying particle-based strain rate (G), number of molecules (scaled to the average number for each pulse; H), appearance rate (I), and disappearance rate (J) versus time. **(K)** Total rate of change in myosin density (green) and the individual contributions to rate of change from turnover (red) and surface contraction (purple). Data in G–K were averaged over 30 pulses, collected in five embryos. Shaded areas represent 95% confidence intervals.

obvious candidate is the small GTPase RhoA (encoded by *rho-1* in *C. elegans*), which recruits and/or activates downstream effectors including formins, Rho Kinase, and Anillin to control F-actin assembly and Myosin II activation in a variety of cell types (Jaffe and Hall, 2005; Piekny and Glotzer, 2008). RhoA activity is required for pulsed contractions in P0 (Motegi and Sugimoto, 2006; Schonegg and Hyman, 2006; Tse et al., 2012), and a biosensor for active RhoA containing the RhoA-binding domain of Anillin (GFP::AHPH) accumulates locally during pulsed contractions in the zygote (Tse et al., 2012; Nishikawa et al., 2017).

To determine the relative timings of RhoA activation and actomyosin accumulation during pulsed contractions, we used a strain coexpressing GFP::AHPH (Tse et al., 2012) with an RFP-tagged version of the myosin heavy chain (NMY-2::RFP) to comonitor RhoA activity and Myosin II accumulation during individual pulses in AB. We observed a striking correlation between pulsed accumulation of GFP::AHPH and NMY-2::RFP during individual pulsed contractions (Fig. 4, A–C; and Video 5). GFP::AHPH accumulated rapidly within a broad domain that prefigured the initial accumulation of NMY-2::RFP, reached a peak near the onset of visible contraction, and then began to disappear before NMY-2::RFP (Fig. 4, B and C). NMY-2::RFP accumulated as discrete particles that increased in number and size, while contracting together into a smaller and tighter central domain. The initial accumulation of GFP::AHPH was diffuse, but over time, a fraction of the total GFP::AHPH became enriched within brighter punctae that colocalized with NMY-2::RFP (Fig. 4 B, yellow arrows). During the falling phase of each pulse, the diffuse pool of GFP::AHPH disappeared rapidly, while a smaller and more persistent fraction of GFP::AHPH remained colocalized with NMY-2::RFP particles (Fig. 4 B, yellow arrows).

To quantify these observations, we aligned data for multiple pulses from embryos coexpressing NMY-2::RFP and GFP::AHPH as follows (Fig. S3; Materials and methods). For each pulse, we smoothed and thresholded the NMY-2::RFP signal to identify a ROI containing high levels of NMY-2::RFP just before the onset of contraction (Fig. S3 A; Materials and methods). We propagated this ROI forward and backward in time (Fig. S3 A). We measured the mean intensities of the NMY-2::RFP and GFP::AHPH signals within the ROI before, during, and after the pulse and normalized these data with respect to the minimum (precontraction) and maximum intensities measured during this interval (Fig. S3 B). Then we aligned data for multiple pulses with respect to the time point at which NMY-2::RFP reached 25% of its maximum intensity (Fig. 4 D and Fig. S3 C). To distinguish different GFP::AHPH fractions, we thresholded the raw NMY-2::RFP signal to create a binary mask that distinguishes regions of high and low Myosin II intensity within the ROI (Fig. S3 D). Then we used this mask to decompose the normalized AHPH::GFP signal into "diffuse" and "myosin-colocalized" fractions (Fig. S3, E and F).

These aligned data confirm that sharp increases and decreases in total GFP::AHPH intensity precede, respectively, the

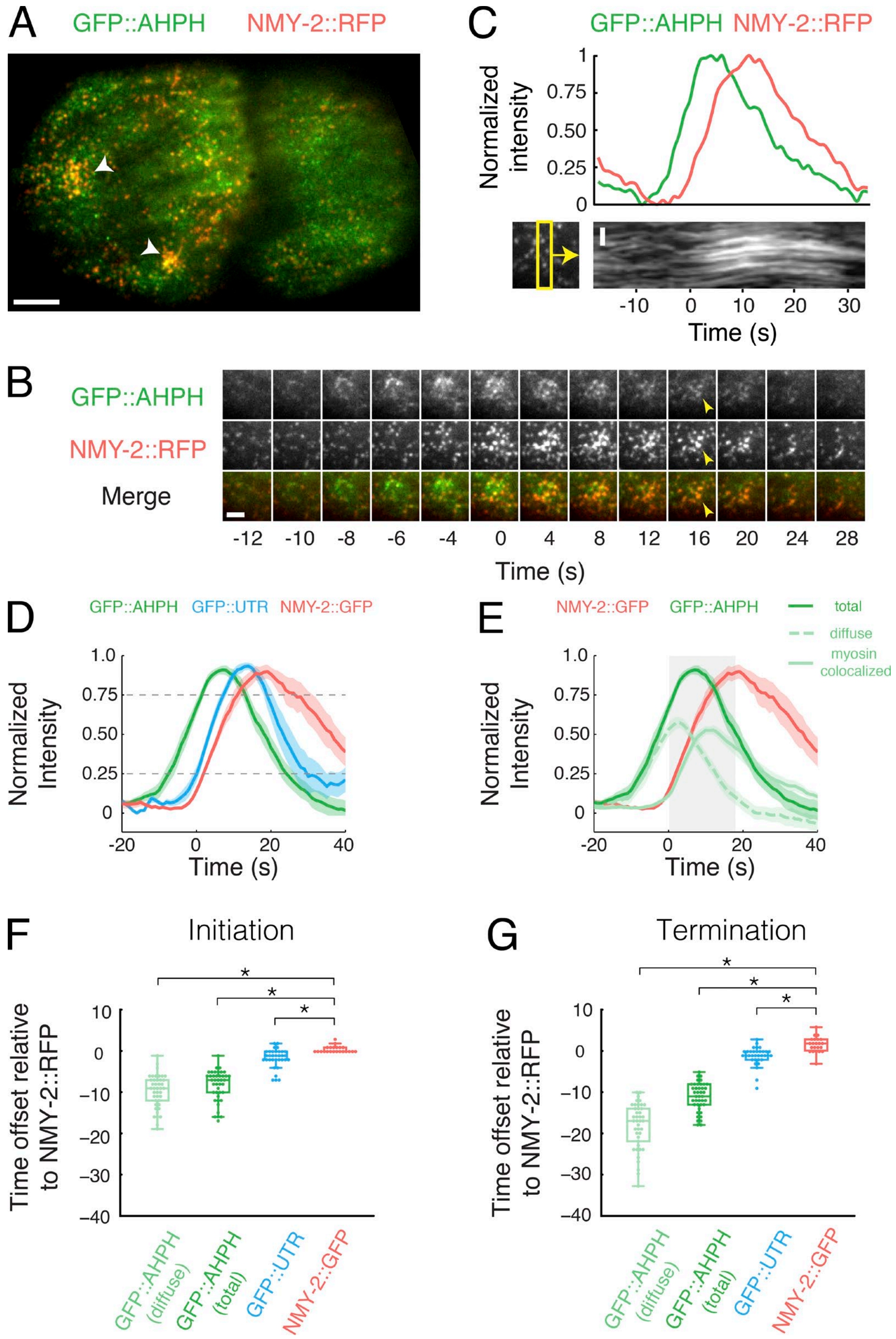

Figure 4. **Local pulses of RhoA activation underlie pulsed accumulation and disappearance of F-actin and Myosin II. (A)** Micrograph of a two-cell–stage embryo expressing GFP::AHPH as a reporter for RhoA activity and NMY-2::RFP. **(B)** Temporal dynamics of GFP::AHPH and NMY-2::RFP accumulation during a single pulse. The time between frames is 2 s for the first five frames and 4 s thereafter. **(C)** Top: Normalized fluorescence intensities of GFP::AHPH and NMY-2::RFP. Bottom: A kymograph showing that local contraction (concerted movements of myosin puncta) begins after the accumulation of GFP::AHPH. The yellow box on the bottom left indicates the region used to generate the kymograph. **(D)** Comparison of averaged normalized fluorescence intensities versus time for active RhoA (GFP::AHPH), Myosin (NMY-2::GFP), and F-actin (GFP::UTR) from two-color data, coaligned with respect to a common reference signal (NMY-2:RFP). Data were coaligned with respect to the time at which NMY-2::RFP reaches 25% threshold. Shaded areas represent 95% confidence intervals. **(E)** Decomposition of the GFP::AHPH signal into a diffuse pool (green dashed line) and myosin-colocalized pool (green solid line; see Fig. S3 and Materials and methods for details). Data for NMY-2::RFP and total GFP::AHPH are the same as in D. **(F)** Distribution of the delays between the onset of accumulation of NMY-2::RFP, and

appearance and disappearance of NMY-2::RFP (Fig. 4 D). On average, total GFP::AHPH reached 25% of its maximum intensity 8.6 ± 3.9 s before NMY-2::RFP (Fig. 4 F) and fell below 75% of its maximum intensity 11.1 ± 3.5 s before NMY-2::RFP (Fig. 4 G). Consistent with direct observations, the mean intensity of the diffuse fraction rose in phase with, but peaked earlier than, the total GFP::AHPH signal, while the mean intensity of the myosin-colocalized fraction rose in phase with NMY-2::RFP and peaked later than the total GFP::AHPH signal (Fig. 4, E–G).

We used the same approach to align data for embryos coexpressing NMY-2::RFP and the F-actin–binding domain of Utrophin (UTR) fused to GFP (GFP::UTR), a marker for F-actin (Burkel et al., 2007; Tse et al., 2012). Using NMY-2::RFP as the common reference to coalign data for NMY-2::RFP, GFP::AHPH, and GFP::UTR, we found that, like Myosin II, F-actin accumulates and dissipates during pulsed contractions with a significant delay relative to GFP::AHPH (Fig. 4, D, F, and G). Thus, local activation and inactivation of RhoA precedes the accumulation and disappearance of its downstream targets.

Finally, we used the time points at which NMY-2::RFP intensities (Fig. 4 D) and single-molecule densities of Myosin::GFP (Fig. 3 H) reached 25% of their peak values to align the time course of GFP::AHPH accumulation with respect to the onset of contraction as measured by single-molecule imaging. This analysis shows that the GFP::AHPH signal peaks just before (diffuse signal) or just after (total signal) the onset of contraction (Fig. 4 E, gray box). Thus, the local concentration of active RhoA by advection-contraction (Munjal et al., 2015) cannot explain the rising phase of RhoA activation in *C. elegans* embryos. Moreover, the diffuse GFP::AHPH signal peaks and begins to fall at a point where F-actin and Myosin II disappearance rates are at a minimum (Fig. 3, D and J); thus, factors other than cortical actomyosin disassembly drive the disappearance of active RhoA at the end of a pulse.

We used the same two-color image analysis to characterize coaccumulation of GFP::AHPH, NMY-2::RFP, and GFP::UTR during pulsed contractions in the P0. To remove the potentially confounding effects of large-scale cortical flows that occur during zygote polarization, we performed these measurements in embryos depleted of the centrosomal factor SPD-5 (Hamill et al., 2002; Munro et al., 2004), which exhibit pulsed contractions but lack cortical flows. In *spd-5(RNAi)* P0s, as in wild-type AB cells, increases in local GFP::AHPH intensity preceded the rise of NMY-2::RFP (Fig. S4, B–D) and to a lesser extent GFP::UTR (Fig. S4 D). As in AB, the initial accumulation of GFP::AHPH was broad and diffuse, while a more persistent pool of punctate GFP::AHPH colocalized with NMY-2::RFP within a more central region of the initial domain (Fig. S4 B, yellow arrows). The duration of GFP::AHPH and NMY-2::RFP accumulation was significantly longer in *spd-5(RNAi)* P0s than in wild-type AB cells. However, decomposition of the GFP::AHPH signal into diffuse and myosin colocalized fractions (Figs. S3 F and S4 E) revealed that the diffuse GFP::AHPH signal rose and fell with very similar temporal dynamics in AB and P0, while the myosin colocalized signal was far more persistent in P0 than in AB (Fig. S3, compare E and F).

Pulsed activation of RhoA does not require Myosin II

The observation that active RhoA peaks before the onset of contraction rules out models in which local contraction concentrates RhoA, or its upstream activators, to initiate pulses (Munjal et al., 2015). However, Myosin II could act in other ways to promote or shape pulsed activation of RhoA. To test this possibility, we used RNAi to deplete NMY-2 in a strain coexpressing transgenic GFP::AHPH and NMY-2 tagged with mKate2 at the endogenous locus by CRISPR-mediated homologous recombination (a gift of Dan Dickinson, University of Texas, Austin, TX). We found that local pulses of GFP::AHPH accumulation persisted in zygotes almost completely depleted of NMY-2, such that fewer than two NMY-2::mKate2-containing particles could be detected during a given pulse (Fig. 5, A and B; and Video 6). Focal accumulations of GFP::AHPH in *nmy-2(RNAi)* zygotes were comparable in size and spacing to those observed in *spd-5 (RNAi)* zygotes. However, the GFP::AHPH signal was entirely diffuse; the punctate signal that colocalizes with Myosin II in wild-type embryos was absent, and the mean time course for GFP::AHPH accumulation and disappearance was very similar to that measured for the diffuse pool of GFP::AHPH both in wild-type AB cells and in *spd-5(RNAi)* zygotes (Fig. 5 C). Assuming the diffuse AHPH signal reflects active RhoA, these data reveal the existence of a mechanism for locally pulsatile activation of RhoA, with similar kinetics in P0 and AB cells, that does not require the presence or activity of Myosin II. Whether the more persistent pool of myosin-colocalized AHPH reflects myosin-dependent recruitment and/or stabilization of active RhoA or binding of the Anillin AHPH domain to other cortical factors remains unclear (see Discussion).

Another key regulator of pulsed contractions is the scaffold anillin, which binds F-actin, Myosin II, active RhoA, and other cortical factors. The *C. elegans* anillin ANI-1 promotes focal accumulations of Myosin II during polarization and cytokinesis (Maddox et al., 2007; Tse et al., 2011), but whether it does so by promoting RhoA activation, or by recruiting/stabilizing Myosin II downstream of RhoA or both remains unclear. To distinguish these possibilities, we first used two-color image analysis to examine the relative timing of GFP::AHPH and GFP::ANI-1 accumulation during individual pulses using NMY-2::RFP as a common reference. In both AB and P0 cells, GFP::ANI-1 accumulated slightly before NMY-2::GFP, and thus with a pronounced delay relative to GFP::AHPH, although the delay was smaller in P0 cells (Fig. 6, A–H). In AB cells, the GFP::AHPH signal reached its maximum rate of accumulation before a

---

the onset of accumulation of GFP::AHPH, NMY-2::GFP, and GFP::UTR. Onset of accumulation was measured as the time at which normalized probe intensity rose above 25% of its maximal level. **(G)** Distribution of the delays between the onset of disappearance of NMY-2:RFP and the onset of disappearance of GFP::AHPH, NMY-2::GFP, and GFP::UTR. The onset of disappearance was measured as the time at which normalized probe intensity fell below 75% of its maximal level. Data in D–G were averaged over the following—GFP::AHPH: *n* = 41 pulses in 7 embryos; GFP::UTR: *n* = 33 pulses in 13 embryos; NMY-2::GFP: *n* = 22 pulses in 4 embryos. In F and G box plots, the central mark represents the median, the box indicates the 25th and 75th percentile, the whiskers mark the minimum and maximum values, + represents outliers, and * indicates statistically significant differences with $P < 0.01$. Bars: (A) 5 µm; (B and C) 2 µm.

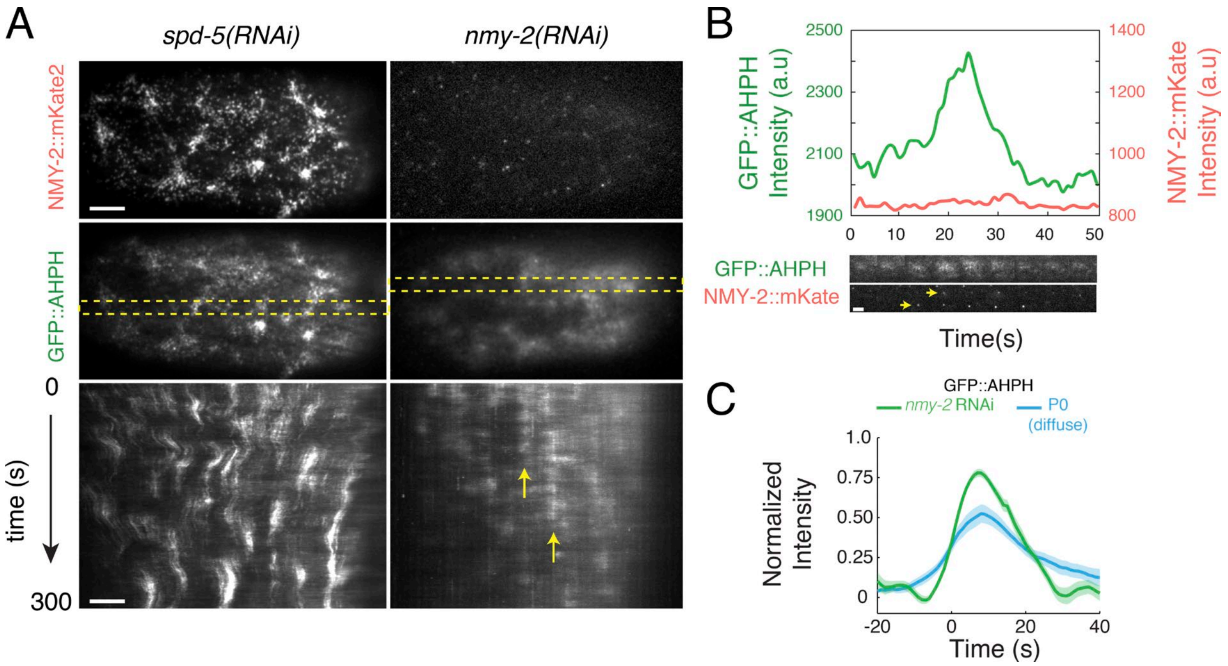

Figure 5. **Myosin II is not required for the pulsed activation of RhoA. (A)** Comparison of pulse dynamics in zygotes expressing GFP::AHPH and NMY-2:: mKATE and treated with either *spd-5(RNAi)* or *nmy-2(RNAi)*. Top panels show myosin localization (NMY-2::mKATE), middle panels show RhoA activity (GFP::AHPH). Bottom panels are kymographs showing GFP::AHPH dynamics over time. Dashed yellow rectangles in middle panel indicate the regions from which the kymographs were made. Vertical yellow arrows indicate a region undergoing repeated pulses. Intensities were scaled identically for *spd-5(RNAi)* and *nmy-2(RNAi)* zygotes. **(B)** Top: Mean intensities of NMY-2::mKATE (red) and GFP::AHPH (green) versus time for a single pulse in an *nmy-2(RNAi)* zygote. Bottom: Sequential snapshots of the region undergoing the pulse showing NMY-2::mKATE (red) and GFP::AHPH (green) distributions. Yellow arrowheads indicate the two particles that can be detected in the region undergoing a pulse. **(C)** Comparison of total GFP::AHPH during pulses in *nmy-2(RNAi)* zygotes (green curve) with the diffuse pool of GFP::AHPH in *spd-5(RNAi)* zygotes (blue curve). For each condition, data were aligned with respect to the time at which the normalized signal reached 25% of its maximum value. Data for diffuse AHPH::GFP in *spd-5(RNAi)* zygotes and wild-type AB cells are identical to those shown in Figs. S4E and 4E, respectively (see Fig. 4 E; Fig. S3, D–F; and Fig. S4 E for details). Data for *nmy-2(RNAi)* in C were averaged over 101 pulses in three embryos. Shaded areas represent 95% confidence intervals. Bars: (A) 5 µm; (B) 2 µm. a.u., arbitrary unit.

detectable increase in GFP::ANI-1 (Fig. 6 C), suggesting that a local increase in ANI-1 is not required for rapid activation of RhoA during pulse initiation.

To test this further, we depleted zygotes of ANI-1 by RNAi in two different ways: RNAi against the full-length ani-1 sequence [*ani-1*$_{FL}$*(RNAi)*] produced strong depletion of both ANI-1 and GFH::AHPH, while RNAi against a shorter N-terminal portion of the ani-1 sequence (*ani-1*$_{N}$*(RNAi)*) produced weaker depletion but without affecting GFP::AHPH expression. In *ani-1*$_{FL}$*(RNAi)* zygotes, we still observed pulsed accumulations of NMY-2::RFP, but the pulse duration was sharply reduced relative to wild-type or *spd-5(RNAi)* zygotes (Fig. S5, I, K, L, and N), consistent with previous reports (Maddox et al., 2007; Tse et al., 2011). In *ani-1*$_{N}$*(RNAi)* zygotes, the duration of NMY-2::RFP pulses was also sharply reduced, although to a lesser extent than in *ani-1*$_{FL}$*(RNAi)* (Fig. 6, J and M). The duration of GFP::AHPH pulses was also strongly reduced, mainly due to the reduction of the myosin-colocalized signal (Fig. 6, J and M). In contrast, the diffuse GFP::AHPH signal rose and fell with kinetics that were very similar to those observed in *spd-5(RNAi)* zygotes (Fig. 6, compare L and M). These data argue against an important role for ANI-1 in promoting activation of RhoA during pulse initiation and instead support a key role for ANI-1 in stabilizing Myosin II downstream of RhoA.

RhoA feeds back locally to promote its own activity, and this is required for pulse initiation

What drives the rapid rise in RhoA activity during pulse initiation? Plotting the rate of change in GFP::AHPH intensity versus intensity during the rising phase of individual pulses in either P0 or AB cells revealed a sharp increase in the rate of RhoA activation with increasing RhoA (Fig. 7 A). This is consistent with a scenario in which active RhoA feeds back positively to promote further activation of RhoA. However, it could also reflect pulsed activation of RhoA (without feedback) by an upstream activator. To distinguish these possibilities, we used RNAi to progressively deplete embryos of RhoA. If the time course of RhoA activation is dictated by an upstream activator, we should observe pulsed accumulation of GFP::AHPH as long as it remains detectable at the cortex. In contrast, if positive feedback of RhoA onto itself drives pulse initiation, then there should be an abrupt loss of pulsing below a threshold level of RhoA. Consistent with the latter expectation, we observed an abrupt transition from pulsed to nonpulsed RhoA accumulation after ~12 h of feeding (Fig. 7, B and C; and Video 7). In zygotes that lacked pulsed RhoA accumulation, we could still readily detect robust RhoA-dependent cortical flows (Motegi and Sugimoto, 2006; Schonegg and Hyman, 2006) during polarity establishment (Fig. 7 B, dashed yellow lines) and localized accumulation of active RhoA before cytokinesis

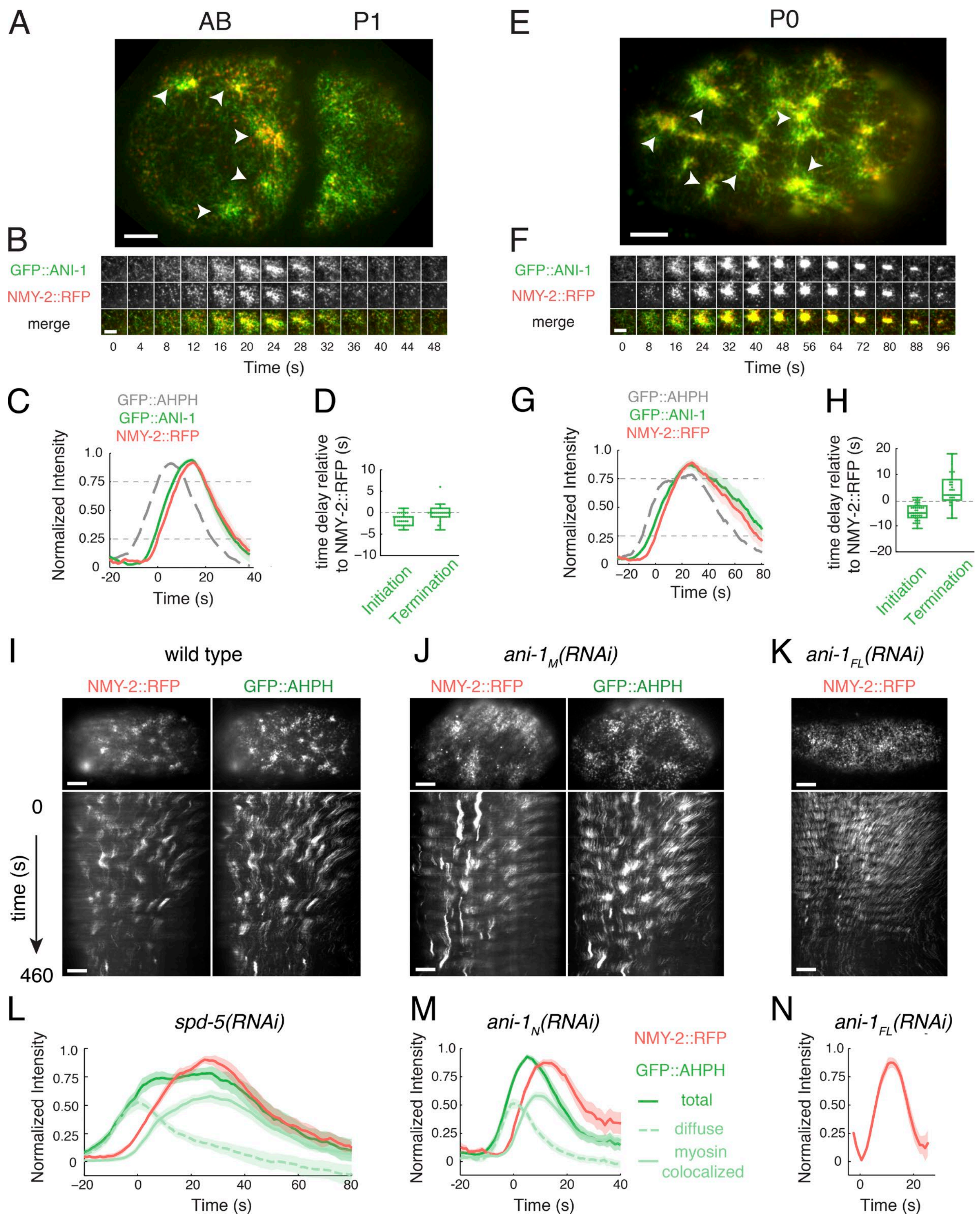

Figure 6. **Two-color analysis of Anillin dynamics and contributions to pulsed contractions in one- and two-cell embryos. (A and E)** Micrographs of two-cell (A) and one-cell (E) embryos coexpressing GFP::ANI-1 and NMY-2::RFP. White arrowheads indicate individual pulses. **(B and F)** Expanded views of single pulses illustrating temporal dynamics of GFP::ANI-1 and NMY-2::RFP accumulation. **(C and G)** Plots of averaged normalized fluorescence intensities for NMY-2::RFP and GFP::ANI-1 from two-color videos, aligned to the time at which NMY-2::RFP reaches 25% threshold. The averaged normalized fluorescence intensity of GFP::AHPH, coaligned by using the NMY-2::RFP signal, is shown for reference. **(D and H)** Distribution of the delays in the onset of appearance and disappearance of GFP::ANI-1 measured relative to NMY-2::RFP. The onset of appearance and disappearance was measured, respectively, as the time at which the normalized signal rose above 25% or fell below 75% of the maximum value. **(I–K)** Single frames (top) and kymographs (bottom) comparing NMY-2::RFP and GFP::AHPH dynamics in (I) wild-type, (J) *ani-1*$_M$*(RNAi)*, and (K) *ani-1*$_{FL}$*(RNAi)* zygotes. **(L and M)** Plots of averaged normalized fluorescence intensities of NMY-2::RFP and GFP::AHPH (total, diffuse, and myosin-colocalized) for individual pulses from two-color videos in (L) *spd-5(RNAi)* and (M) *ani-1*$_M$*(RNAi)* zygotes, aligned to the time at which NMY-2::RFP reaches 25% threshold. Data in L are identical to those shown in Fig. S4 E. **(N)** Plots of averaged normalized

(Fig. 7 B, cyan arrowheads). Together, these observations support the idea that RhoA feeds back positively to amplify its own activation and that sufficiently strong feedback is required to generate local pulses of high RhoA activity.

Delayed accumulation of the Rho GAPs RGA-3/4 underlies pulse termination

What terminates RhoA activity during each pulse? Our results imply that local termination of RhoA activity at the end of a pulse does not require Myosin II activity or (by extension) its local inhibition by Myosin phosphatase (Piekny and Mains, 2002; Piekny et al., 2003; Diogon et al., 2007), nor is it timed by cortical disassembly. Previous studies identified the redundant RhoA GAPs RGA-3 and RGA-4 as inhibitors of RhoA activity during polarization and cytokinesis (Schmutz et al., 2007; Schonegg et al., 2007; Tse et al., 2012; Zanin et al., 2013). A YFP-tagged RGA-3 transgene accumulates at the cortex in early embryos (Schonegg et al., 2007), and simultaneous depletion of RGA-3 and RGA-4 leads to hyper activation of RhoA and hypercontractility during zygotic polarization (Schmutz et al., 2007; Schonegg et al., 2007; Tse et al., 2012). We wondered, therefore, if RGA-3/4 could provide delayed negative feedback to terminate RhoA activity during individual pulses.

To test this possibility, we first imaged embryos coexpressing GFP::RGA-3 (Zanin et al., 2013) and NMY-2::mKATE. Focusing on AB, and using two-color analysis as above, we confirmed that GFP::RGA-3 is present throughout the cortex but accumulates locally during individual pulsed contractions (Fig. 8, A–C; and Video 8). Significantly, GFP::RGA-3 and NMY-2::mKATE accumulated with very similar timing (Fig. 8 B). Using NMY-2::mKATE and NMY-2::RFP as common signals to co-align data for GFP::AHPH and GFP::RGA-3, we inferred that GFP::RGA-3 accumulates with an ~6-s delay relative to GFP::AHPH, the rate of RhoA activation peaks before the onset of GFP::RGA-3 accumulation, and rapid accumulation of GFP::RGA-3 coincides with deceleration and then reversal of RhoA activation (Fig. 8 C, bottom). Together, these observations suggest that delayed accumulation of RGA-3/4 plays a key role in terminating each pulse of RhoA activity. To test this further, we created a strain in which GFP::AHPH and NMY-2::mKATE were coexpressed in *rga-3; rga-4* (*rga-3/4*) double-mutant embryos (Zanin et al., 2013). Consistent with previous reports (Schmutz et al., 2007; Schonegg et al., 2007; Tse et al., 2012; Zanin et al., 2013), during polarity establishment in *rga-3/4* double-mutant zygotes, we observed hyperaccumulation of GFP::AHPH and hypercontractility, characterized by convulsive contractions of the anterior cortex and rapid anterior-directed cortical flows (Fig. 8 D, second column; and Video 9). However, we could no longer detect local pulses of GFP::AHPH in these embryos. To exclude the possibility that rapid flows sequester factors required for pulsed contractility to the extreme anterior pole, we used partial depletion of the myosin regulatory light chain (MLC-4) to attenuate contractility and cortical flows in *rga-3/4* double-mutant zygotes or in control zygotes that were doubly heterozygous for *rga-3* and *rga-4* (Fig. 8 D and Video 9). In *rga-3/4* heterozygotes partially depleted of MLC-4, cortical flows were sharply reduced, but pulsed accumulation of GFP::AHPH could be readily detected (Fig. 8 D, third column; and Video 9). In contrast, in *rga-3/4* double-mutant zygotes partially depleted of MLC-4, cortical flows during the polarity establishment phase were slower than observed in wild-type embryos; GFP::AHPH was uniformly enriched, but we did not observe local pulses of GFP::AHPH accumulation (Fig. 8 D, fourth column; and Video 9). Together, these data suggest that negative feedback through delayed accumulation of RGA-3/4 plays a key role in terminating local pulses of RhoA activity.

RGA-3/4 colocalizes with F-actin and requires F-actin for cortical association

Recent work suggests that F-actin accumulation inhibits RhoA activity to promote excitable dynamics in echinoderm and frog oocytes and embryos (Bement et al., 2015). We wondered if F-actin might play a similar role in *C. elegans* embryos by promoting recruitment of RGA-3/4. Consistent with this possibility, two-color live imaging of embryos coexpressing GFP::RGA-3 and mCherry::Lifeact (a marker for F-actin; Pohl et al., 2012) revealed extensive overlap of GFP::RGA-3 and mCherry::Lifeact signals throughout the cortex (Fig. 9, A and D) and during individual pulses (Fig. 9, B and E) in both AB and P0 cells. Scatterplots showing a pixelwise comparison of the two signals (Fig. 9, C and F) and measurements of Pearson's r and Mander's (M_{RGA}) correlation coefficients over the entire cortex (P0: r = 0.9, M_{RGA} = 0.98; AB: r = 0.8, M_{RGA} = 0.96) or during individual pulses (P0: r = 0.84 ± 0.03, M_{RGA} = 0.97 ± 0.02; AB: r = 0.65 ± 0.05, M_{RGA} = 0.89 ± 0.03; mean ± SD; *n* = 10 pulses) confirmed strong colocalization.

To test whether F-actin is required for cortical localization of GFP::RGA-3, we treated permeabilized zygotes (Carvalho et al., 2011; Olson et al., 2012) coexpressing mCherry::Lifeact and GFP::RGA-3 with Latrunculin A (LatA) to rapidly depolymerize F-actin. Acute treatment with 10 µM LatA led to a rapid collapse of the cortical F-actin network and complete disappearance of F-actin from the cortex within ~60 s. GFP::RGA-3 disappeared from the cortex with nearly identical timing and remained closely associated with the F-actin network as it collapsed (Fig. 9 G and Video 10; *n* = 6 embryos). These data suggest that cortical localization of RGA-3 depends on continuous physical association with F-actin. In contrast, upon acute depolymerization of F-actin, RFP::NMY-2, GFP-AHPH, GFP::Anillin, and GFP::Septin became rapidly enriched within dense punctate structures (Fig. 9 H; Fig. S5, A and B; and data not shown), similar to what has previously been described in other contexts (Hickson and O'Farrell, 2008), suggesting that none of these other downstream targets of RhoA are sufficient for cortical recruitment of RGA-3 (at least in the absence of an intact cortical actin network).

We could no longer detect pulsed accumulation of AHPH after acute treatment of permeabilized zygotes with LatA. However,

fluorescence intensities of NMY-2::RFP for individual pulses in *ani-1*$_{FL}$*(RNAi)* zygotes, aligned to the time at which NMY-2::RFP reaches 25% threshold. Data in C–L were averaged over the following—C and D: 35 pulses in 10 embryos; G and H: 42 pulses in 4 embryos; I and L: 40 pulses in 3 embryos; J and M: 51 pulses in 4 embryos; K and N: 43 pulses in 3 embryos. Shaded areas represent 95% confidence intervals. Bars: (A, E, I, and K) 5 µm; (B and F) 3 µm.

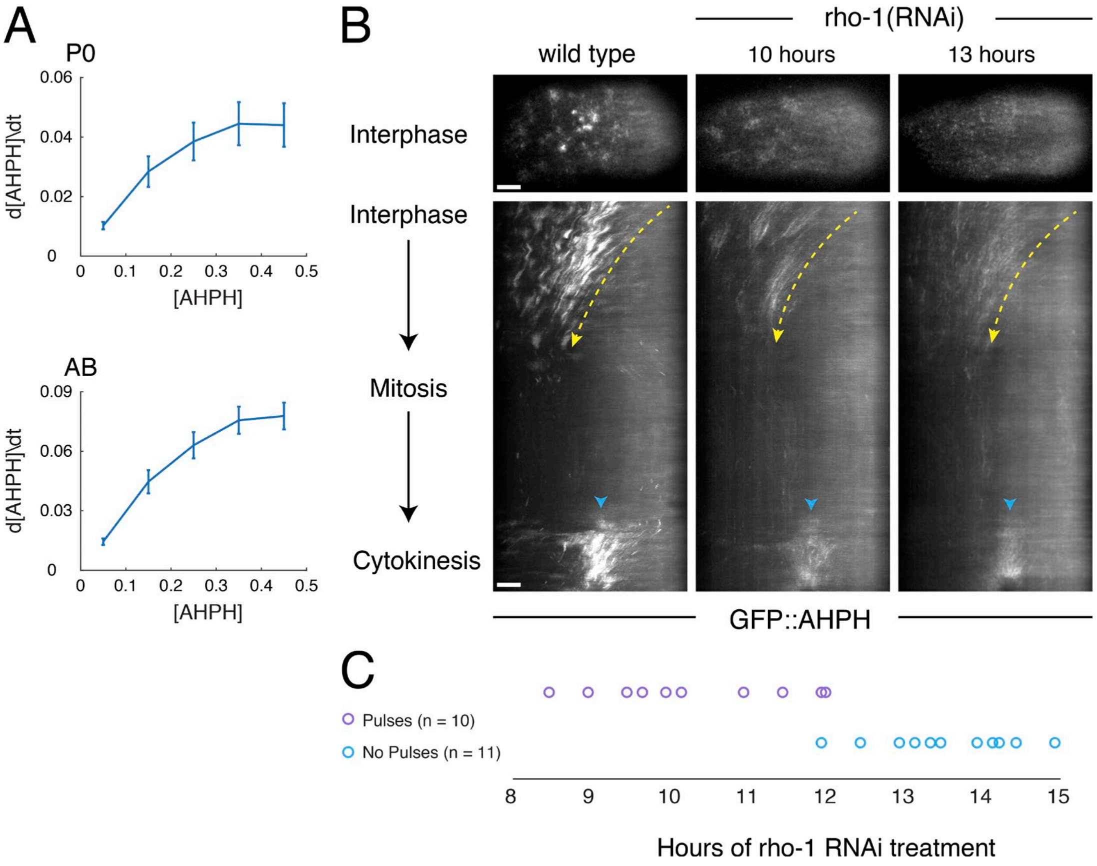

Figure 7. **RhoA activation is autocatalytic. (A)** The time derivative of normalized RhoA activity (GFP::AHPH) plotted versus normalized activity during the early phase of pulse initiation in the P0 (top: $n = 40$ pulses in four embryos) and AB (bottom: $n = 41$ pulses in seven embryos). Error bars indicate 95% confidence interval. **(B and C)** Analysis of pulse dynamics in embryos progressively depleted of RHO-1 by RNAi. **(B)** Top panels show GFP::AHPH distributions in interphase embryos from mothers subjected to no (wild-type), 10 h, and 13 h of *rho-1(RNAi)*. Middle panels show kymographs from the same embryos illustrating spatiotemporal dynamics of GFP::AHPH from interphase through cytokinesis. Dashed yellow lines indicate approximate pattern of cortical flow. Cyan arrowheads indicate accumulation of GFP::AHPH just before cytokinesis. **(C)** Timeline indicating the presence (magenta circles) or absence (cyan circles) of pulsing in embryos treated with *rho-1(RNAi)* for the indicated times, revealing an abrupt transition from pulsing to no pulsing at ~12 h after treatment. Bars, 5 µm.

this could be due to the sequestration of RhoA itself, or the biosensor, into dense clusters, as described above. We found that GFP::AHPH was no longer enriched in dense clusters after LatA treatment in embryos mutant for the Septin *unc-59* (Fig. 9 I). Pulsed accumulation of GFP::AHPH and NMY-2::RFP persisted in *unc-59*-mutant zygotes (Fig. S5, D and E). However, acute treatment of permeabilized *unc-59* zygotes with LatA lead to rapid accumulation of a diffuse pool of GFP::AHPH throughout the cortex and a loss of pulsing (Fig. 9 I), analogous to what we observed in *rga-3/4* double-mutant zygotes.

Fast positive and delayed negative feedback involving RhoA and RGA-3/4 can account quantitatively for locally pulsatile RhoA dynamics

Our data suggest that in the early *C. elegans* embryo, locally excitable RhoA dynamics arise independently of myosin activity through a combination of fast positive feedback on RhoA activity and delayed negative feedback via local F-actin–dependent recruitment of RGA-3/4 (Fig. 10 A). To test this idea, we asked if a simple model based on these feedbacks with parameters constrained by experimental measurements predicts excitable dynamics. We formulated the model as a pair of ordinary differential equations, describing local rates of change in active RhoA and RGA-3/4, based on the following assumptions: (a) RhoA is activated at a basal rate and feeds back positively to promote further RhoA activation, (b) RhoA feeds forward through F-actin assembly to promote local, reversible association of RGA-3/4 with the cortex, and (c) RGA-3/4 acts as a GAP to promote local inactivation of RhoA (see Materials and methods for modeling details). Consistent with our experimental observations (Fig. 6 A and Fig. 10, B and C), we assumed that autoactivation of RhoA is a saturating function of RhoA activity, represented by a Hill function with Hill coefficient $n = 1$. We assumed that inactivation of RhoA by RGA-3/4 obeys Michaelis-Menten kinetics. To account for the observed delay between an increase in RhoA and the sharp onset of RGA-3/4 accumulation (Fig. 7 C), we assumed an ultrasensitive dependence of RGA-3/4 accumulation rate on RhoA, with the steepness of the response governed by an exponent m (see Materials and methods for mathematical details).

We set values for basal RhoA activation and RGA-3/4 recruitment rates to very low values, based on the slow rates of increase in GFP::AHPH and GFP::RGA-3 observed before the sharp upswing of each pulse (Fig. 7 C). Then we estimated values for the model's remaining parameters by fitting the right-hand sides of

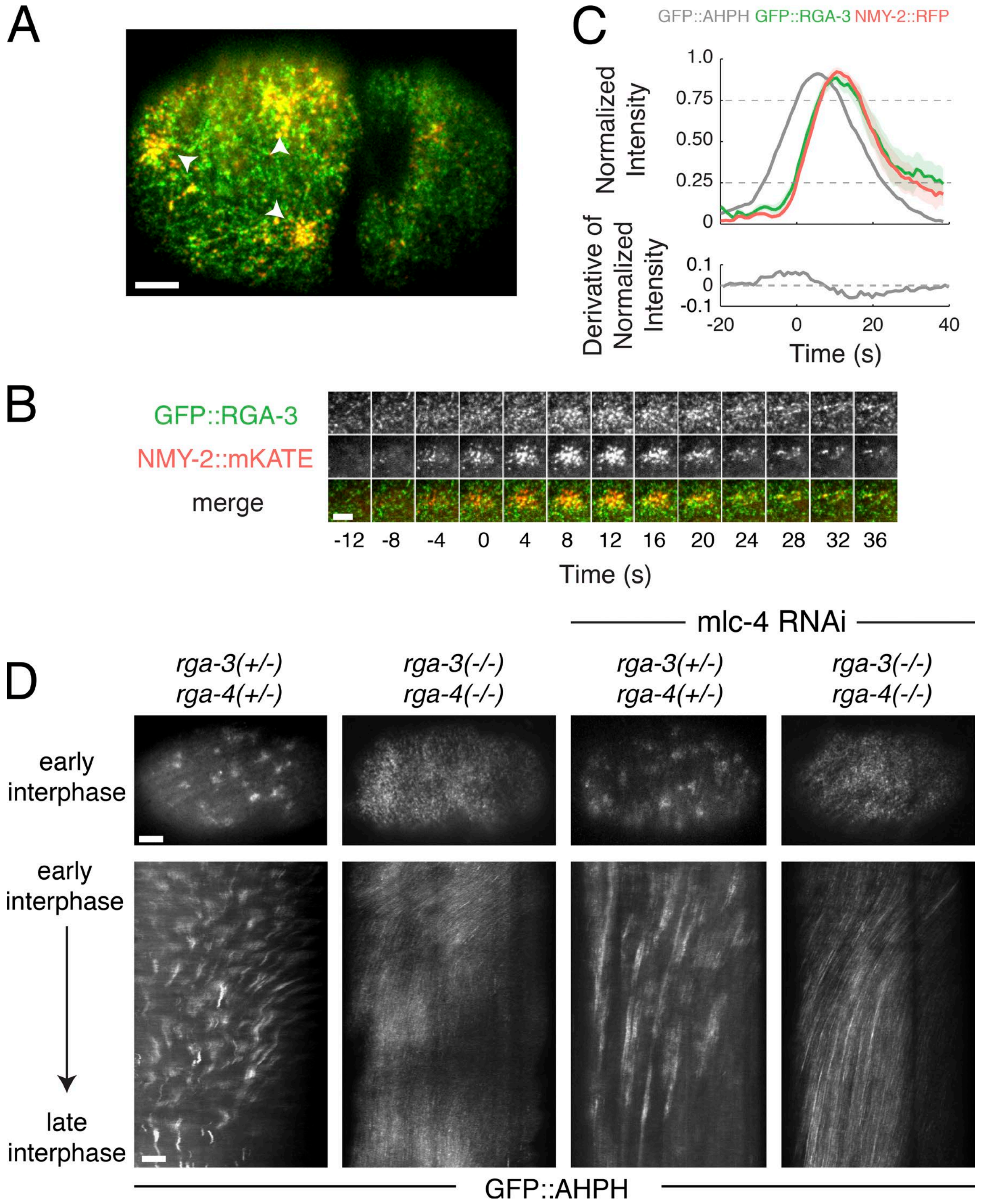

Figure 8. **Delayed accumulation of RGA-3/4 mediates negative feedback required for pulse termination. (A)** Micrograph of a two-cell–stage embryo expressing GFP::RGA-3 (green) and NMY-2::RFP (red). **(B)** Temporal dynamics of a single pulse. **(C)** Top: Averaged normalized fluorescence intensities versus time for NMY-2::RFP and GFP::RGA-3 from two-color data, coaligned with respect to the time at which NMY-2::RFP reaches 25% threshold. The averaged normalized fluorescence intensity of GFP::AHPH, coaligned with NMY-2::RFP. Bottom: The averaged time derivative of the normalized GFP::AHPH intensity, again coaligned by using NMY-2::RFP. Data were averaged over 31 pulses in four embryos. Shaded regions represent 95% confidence intervals. **(D)** Top: Distributions of GFP::AHPH during interphase in zygotes with the indicated genotypes. Bottom: Kymographs showing patterns of GFP::AHPH distribution and redistribution during interphase for the same genotypes. Bars: (A and D) 5 µm; (B) 3 µm.

the model equations to the relationships between dRhoA/dt and dRGA-3/4/dt and RhoA and RGA-3/4, inferred from coaligned, averaged, and normalized GFP::AHPH and GFP::RGA-3 intensities (Fig. 10, B–G; see Materials and methods for details).

Given these parameter estimates, and depending on the exact values chosen for the basal RhoA activation and RGA-3/4 association rates, we observed one of two closely related behaviors: excitable dynamics, characterized by a stable rest state (low RhoA

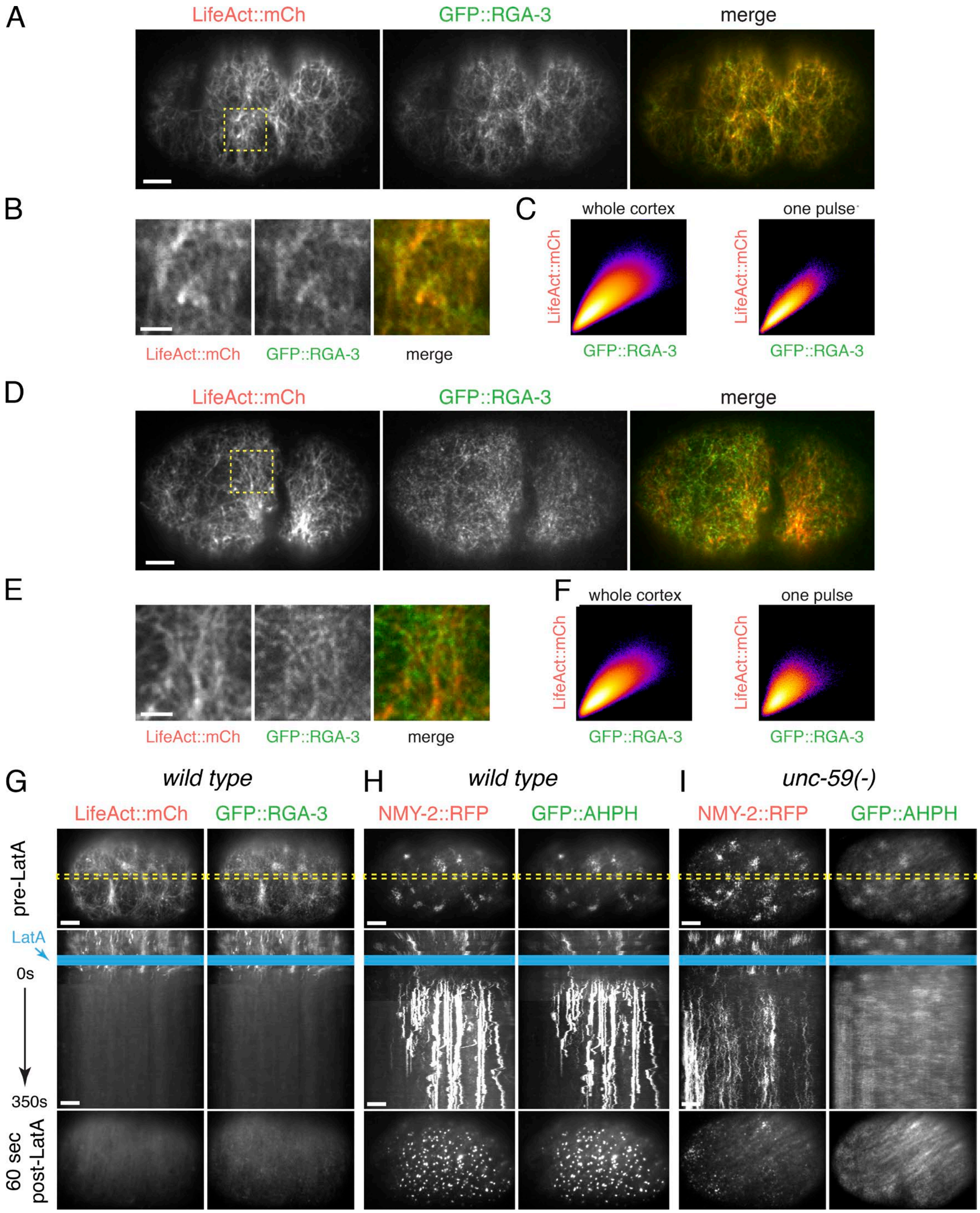

Figure 9. **Cortical RGA-3/4 localization depends on F-actin. (A)** Micrographs of a zygote coexpressing GFP::RGA-3 and mCherry::LifeAct. **(B)** Magnified view of the region indicated by the dashed yellow box in A. **(C)** Scatter plots showing pixel-wise comparisons of GFP::RGA-3 and mCherry::LifeAct intensities for (left) the entire image shown in A or (right) for the duration of a pulse in the ROI shown in B. **(D)** Micrographs of a two-cell embryo coexpressing GFP::RGA-3 and mCherry::LifeAct. **(E)** Magnified view of the region indicated by the dashed yellow box in D. **(F)** Scatter plots showing pixel-wise comparisons of GFP::RGA-3 and mCherry::LifeAct intensities for (left) the entire image shown in E or (right) for the duration of a pulse in the ROI shown in E. **(G)** Wild-type zygote coexpressing GFP::AHPH and mRFP::LifeAct before (top) and ~90 s after (bottom) treatment with 10 µM LatA. Middle panel shows a kymograph taken from the region indicated by the dashed yellow box in the top (pre-LA) micrograph. Blue rectangle indicates time of application of LatA. **(H)** Wild-type zygote coexpressing GFP::AHPH and mRFP::Myosin II before (top) and ~90 s after (bottom) treatment with 10 µM LatA. Kymograph format as in G. **(I)** Homozygous *unc-59*(e261) mutant zygote coexpressing GFP::AHPH and NMY-2::RFP before (top) and ~90 s after (bottom) treatment with 10 µM LatA. Kymograph format as in G. Bars: (A, D, and G–I) 5 µm; (B and E) 2 µm.

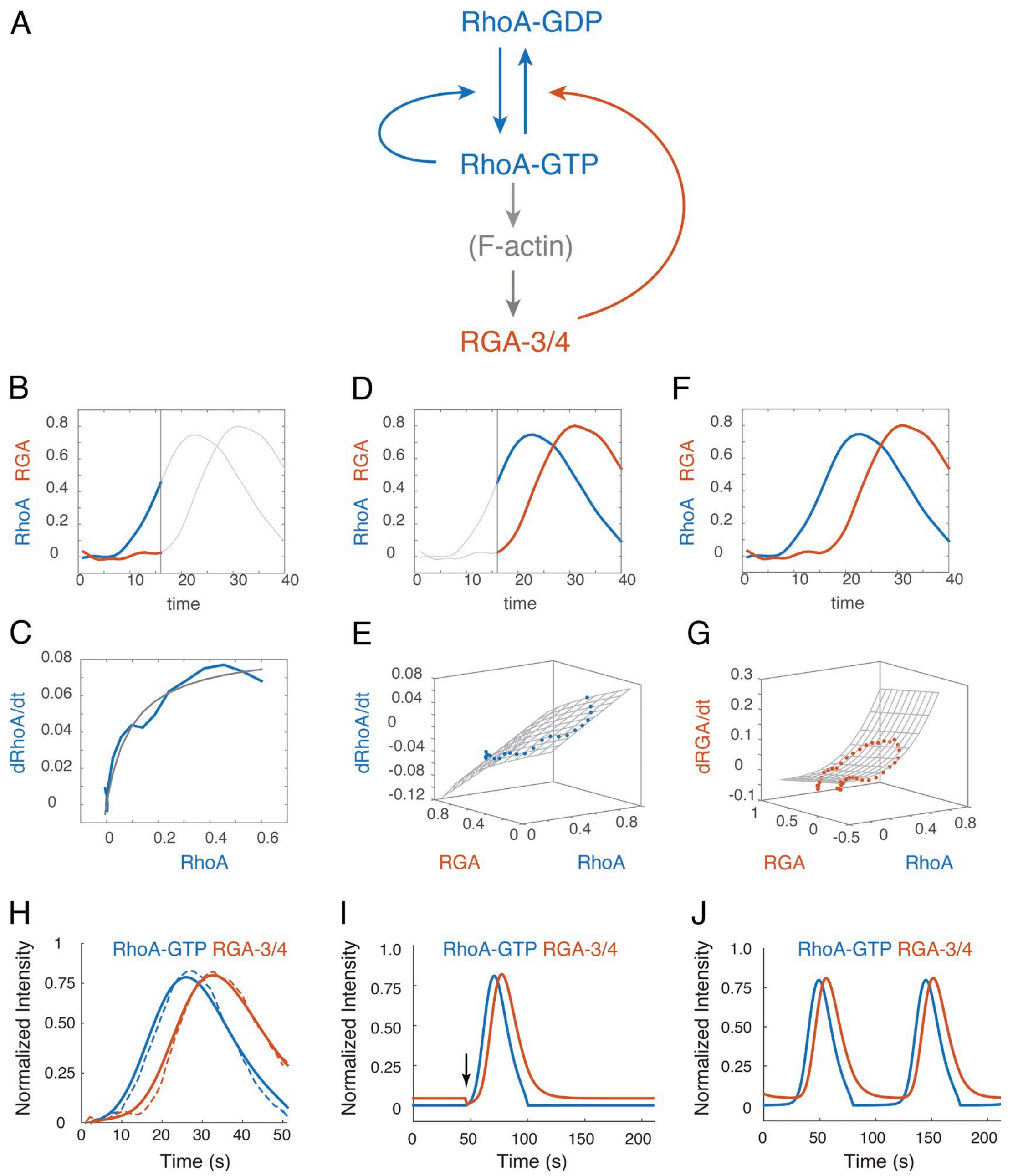

Figure 10. **Autocatalytic RhoA activation and delayed negative feedback through RGA-3/4 is sufficient to produce locally excitable RhoA dynamics.** **(A)** Schematic representation of a simple mathematical model for RhoA pulse dynamics, based on our results. **(B and C)** Fitting the model to measurements of dRhoA/dt versus RhoA during the rising phase of the pulse (colored traces in B; fit shown in C) to estimate the values of parameters governing autoactivation of RhoA. **(D and E)** Fitting the model to measurements of dRhoA/dt versus RhoA and RGA-3 during the later phase of the pulse (colored traces in D; fit shown in E) to estimate the values of parameters governing inhibition of RhoA by RGA-3. **(F and G)** Fitting the model to measurements of dRGA-3/dt versus RhoA and RGA-3 during the entire pulse (colored traces in F; fit shown in G) to estimate the values of parameters governing cortical association and disassociation of RGA-3. See Materials and methods for details of fitting procedures. **(H)** Comparison between measured (dashed lines) and simulated (solid lines) pulse dynamics for the case in which $n = 1$, $k_r^0 = 0.001$, $k_p^0 = 0.0001$, $K_{GAP} = 0.001$, and the remaining model parameters estimated by fitting data are $m = 3.02$, $k_p^{fb} = 0.094$, $K_{fb} = 0.12$, $k_r^{ass} = 0.245$, and $k_r^{diss} = 0.047$ (see Materials and methods for details). **(I)** Simulated dynamics for the parameter values in H are excitable, and a stable rest state can be destabilized by a transient reduction of RGA-3/4 (vertical black arrow) to trigger a single pulse of RhoA activity. **(J)** A small change in the basal RGA-3 association rate from $k_p^0 = 0.0001$ to $k_p^0 = 0.001$ results in oscillatory dynamics, with pulses occurring at regular intervals.

and low RGA), from which the system can be induced to generate a transient pulse by a small decrease in RGA (Fig. 9 B) or a small increase in RhoA (not shown), and oscillatory dynamics, in which the stable rest state is lost and the system undergoes transient pulses at regular intervals (Fig. 9 C). The transition from excitable to oscillatory dynamics could be induced by either a small increase in basal RhoA activation or a small decrease in basal RGA activation. This is consistent with our observations in *nmy-2(RNAi)* embryos that some patches of cortex are quiescent while others exhibit repeated pulses of activity at regular intervals (Fig. 5 A, yellow arrows) and suggests that, in the absence of contractility, the *C. elegans* cortex may be poised close to a transition between excitable (with a low threshold for excitation) and oscillatory dynamics. We conclude that a simple combination of positive and negative feedback loops, coupling local RhoA activity and RGA-3/4 accumulation, is in principle sufficient to explain pulsatile RhoA dynamics in early *C. elegans* embryos, independent of actomyosin contractility.

Discussion

Pulsed contractility is a widespread mode of actomyosin contractility, but its mechanistic basis has remained poorly understood (Levayer and Lecuit, 2012; Gorfinkiel, 2016). Current models for pulsed contractility invoke mechanochemical feedback in which contractile forces produced by Myosin II couple in different ways with actomyosin assembly/disassembly to drive excitable or oscillatory dynamics. Proposed feedback mechanisms include tension-dependent motor-binding kinetics (Effler et al., 2006; Ren et al., 2009; He et al., 2010; Luo et al., 2012), tension-dependent filament assembly/stabilization (Hayakawa et al., 2011; De La Cruz and Gardel, 2015) or disassembly (Machado et al., 2014), tension-dependent activation of Myosin II via, e.g., Ca^{2+} (Kapustina et al., 2008) or RhoA (Koride et al., 2014), or modes of feedback in which local contraction advects and concentrates actomyosin and/or its upstream activators (Bois et al., 2011; Kumar et al., 2014; Munjal et al., 2015; Nishikawa et al., 2017). Here, we have identified a mechanism for pulse generation in early *C. elegans* embryos that does not require force production or redistribution of cortical factors by Myosin II. Using single molecule imaging and particle tracking analysis, we have shown that the rapid initial accumulation of F-actin and Myosin II begins well before the onset of contraction, at a time when the cortex is locally expanding. Redistribution of actomyosin by local contraction makes a minor contribution to the overall accumulation of actomyosin during each pulse. Instead, our data show that pulsed accumulation and disappearance of F-actin and Myosin II are determined primarily by local modulation of their assembly/recruitment and disassembly. Using two-color imaging, we have shown that, during each pulse, a biosensor for active RhoA begins to accumulate well before RhoA's downstream targets F-actin, Myosin II, and Anillin. Active RhoA nearly reaches its peak level before the onset of contraction (Fig. 4 D), and then it begins to disappear well before its downstream targets. Significantly, locally pulsed activation of RhoA continues to occur on patches of cortex that contain only a few (one to two) particles of Myosin II, too few to produce significant local contractile stress. Thus a Myosin-independent RhoA pulse generator underlies pulsed contractility in early *C. elegans* embryos.

One important caveat is that the ANI-1 AHPH domain may bind septin, lipids, or other cortical targets in addition to active RhoA (Piekny and Maddox, 2010). Indeed, we observe what appears to be two phases of AHPH accumulation—a diffuse phase that accumulates early and a second phase that accumulates later and colocalizes with NMY-2. The diffuse pool is likely to reflect RhoA-GTP that is available to bind RhoA affectors. Whether the myosin-colocalized pool bids active RhoA or other cortical factors remains unclear. Importantly, the diffuse pool has very similar kinetics in wild-type AB and in polarization-deficient or myosin-depleted P0 cells, supporting the conclusion that a common myosin-independent mechanism for pulsed activation of RhoA operates in both P0 and AB cells.

The pulses of RhoA activity described here and in other contexts (Bement et al., 2015; Munjal et al., 2015; Mason et al., 2016) are strikingly reminiscent of excitable behaviors found in other systems, such as action potentials in neuronal (Izhikevich, 2007) or cardiac cells (Luo and Rudy, 1991), transient pulses of intracellular calcium release (Goldbeter, 1996), or pulses of actin assembly observed in motile cells (Weiner et al., 2007). Theoretical studies highlight two key ingredients for excitable dynamics: fast positive feedback and delayed negative feedback (Strogatz, 1994). The sharp acceleration of active RhoA accumulation that we observed during the early rising phase of individual pulses is a dynamic signature of fast positive feedback in which RhoA promotes its own activity. Stronger evidence that RhoA participates in a positive feedback loop that is essential for pulsing comes from our observation that depletion of RhoA below a certain threshold leads to an abrupt loss of pulsed contractions while having minimal effects on other RhoA-dependent functions, such as cortical flow during polarization (Motegi and Sugimoto, 2006; Schonegg and Hyman, 2006) or cytokinesis (Loria et al., 2012).

The mechanism for this feedback remains unclear. In AB cells, the rapid acceleration of RhoA activation during pulse initiation occurs before any visible accumulation of Myosin II, Anillin, or F-actin, and in P0, depletion of NMY-2 or ANI-1 has little effect on the rising phase of RhoA activation. Thus, with the possible exception of F-actin in P0, it seems very unlikely that accumulation of these downstream targets makes a significant contribution to positive feedback. A more likely possibility is that RhoA feeds back through one or more of its upstream activators, such as ECT-2, CYK-4, and NOP-1 (Tse et al., 2012). In the zygote, pulsing is sensitive to depletion of ECT-2 and NOP-1 (Tse et al., 2012; Naganathan et al., 2014). During cytokinesis, active RhoA can act as a cofactor to promote transactivation of the RhoGEF ECT-2 by the RhoGAP CYK-4 (Zhang and Glotzer, 2015). While CYK-4 is not required for pulsed activation of RhoA during polarization, it is possible that RhoA could feed back through NOP-1, a protein of unknown activity that is required for RhoA activation during interphase in P0 and AB (Tse et al., 2012). Identifying the molecular mechanism(s) for this feedback is an important goal for future studies.

Regarding delayed negative feedback, direct comparison of our single-molecule and two-color imaging data (compare Figs. 3 and 4) argues strongly against a mechanism in which pulses are terminated by actomyosin disassembly. Both total and diffuse GFP::AHPH signals peak and begin to fall sharply at a time when F-actin and Myosin II disassembly rates are lowest (compare Figs. 3 and 4). Indeed, our data suggest that local accumulation of ANI-1 downstream of RhoA stabilizes Myosin II (and possibly also F-actin) to prolong the contraction phase of each pulse. Instead, our data suggest that the redundantly acting RhoGAPs RGA-3/4 play a key role in providing the delayed negative feedback that terminates RhoA pulses. RGA-3/4 act as GAPs toward RHO-1 in vitro (Schonegg et al., 2007), and loss of RGA-3/4 leads to hyperactivation of RhoA in vivo (Tse et al., 2012). We find that during each pulse, RGA-3 accumulates with a delay of ∼6 s relative to active RhoA. Significantly, the rate of active RhoA accumulation peaks and begins to fall just as GFP::RGA-3 begins to accumulate, suggesting that rapid accumulation of RGA-3/4 plays a key role in timing the end of each RhoA pulse. Consistent with this possibility, RhoA activity is uniformly high, and pulsatile RhoA activation is completely abolished, in *rga-3/4* double-mutant zygotes, even when contractility is attenuated to prevent sequestration of RhoA activators by hyperactive cortical flow. Whether factors other than RGA-3/4 contribute to terminating RhoA pulses remains unclear.

Together, these data suggest a model for locally excitable RhoA dynamics in which RhoA feeds back positively to promote its own activation and feeds back negatively with a delay through RGA-3/4 to promote its own inactivation. Indeed, when we formulate this model mathematically and constrain model parameter values to match the local dependencies of RhoA and RGA-3/4 accumulation rates on levels of RhoA and RGA-3/4 inferred from two-color imaging data, the model predicts locally pulsatile RhoA dynamics, and small tunings of the model's parameters mediate interconversion between excitable dynamics and spontaneous oscillations. This simple modeling exercise establishes an internally consistent hypothesis for pulsatile contractility that can be confirmed and extended by future experiments.

What governs the recruitment of RGA-3/4 during each pulse? We found that GFP::RGA-3 colocalizes broadly and extensively with cortical F-actin in both P0 and AB. RGA-3/4 accumulates with the same timing as F-actin during each pulse, and depolymerizating F-actin abolishes this accumulation. This suggests a specific mechanism for delayed recruitment of RGA-3/4 in which RhoA promotes increased local F-actin assembly (potentially through the formin Cyk-1 [Severson et al., 2002]), and F-actin in turn recruits RGA-3/4. Interestingly, a recent study (Bement et al., 2015) suggests that RhoA and cortical F-actin form an excitable circuit, with RhoA as activator and F-actin as inhibitor, that propagates cortical waves of RhoA activity and F-actin assembly in oocytes and embryonic cells of frogs and echinoderms. The mechanism by which F-actin feeds back to inactivate RhoA in these cells remains unknown, but our observations in *C. elegans* support the idea, proposed by Bement et al. (2015), that a RhoGAP homologous (or analogous) to RGA-3/4 may be recruited by F-actin to mediate negative feedback in frog and echinoderm cells. A similar mechanism has recently been reported in the context of secreting in *Drosophila melanogaster* larval salivary glands (Segal et al., 2018), and a similar circuit design may underlie the propagation of actin waves observed in many motile cells (Allard and Mogilner, 2013).

It is also interesting to compare our observations to those made recently in the *Drosophila* germband (Munjal et al., 2015). In germband cells, pulsed accumulation of a biosensor (GFP fused to the AHPH domain of *Drosophila* anillin) appears to coincide with the local accumulation of F-actin and Myosin II and with the onset of contraction, and it is abolished by inhibition of Rho Kinase, an upstream activator of Myosin II. In *C. elegans*, by contrast, pulsed accumulation of GFP::AHPH precedes actomyosin accumulation and the onset of contraction by many seconds and persists in the almost complete absence of Myosin II.

To some extent, these differences could reflect the imaging methods used to detect the RhoA biosensor. Using near-TIRF imaging in *C. elegans* embryos, we detected two pools of the biosensor: a diffuse pool that begins to accumulate well before Myosin II and a second more punctate pool whose distribution strongly overlaps with Myosin II (Fig. 4 B; Fig. S3, F and G; and Fig. S5). Based on studies in other cells (Weiner et al., 2007), the diffuse pool may be more difficult to detect with the use of confocal microscopy. Thus, it remains possible that a diffuse pool of active RhoA accumulates before actomyosin in the *Drosophila* germband but escapes detection by confocal microscopy.

An alternative idea is that pulsed contractility is governed by locally excitable RhoA dynamics in both systems, but that different forms of positive feedback may contribute differently to driving the rapid upswing of RhoA activity, and that different mechanisms may operate to trigger pulses (by driving RhoA activity above a threshold for excitation). For example, in the *Drosophila* germband, a mode of feedback in which local contraction advects and concentrates active RhoA (or upstream activators) may be required to initiate pulses, whereas in *C. elegans*, local fluctuations in RhoA or RGA-3/4 levels may be sufficient to do so in the absence of contractility. Importantly, in the *Drosophila* germband, as in *C. elegans*, advection/contraction coupling accounts for only a fraction of the total accumulation of active RhoA during each pulse; thus, other modes of positive feedback must also make a significant contribution.

More generally, we hypothesize that the different modes of RhoA excitability that have been described in frog, echinoderm, *C. elegans* and *Drosophila* embryos share a deeper underlying mechanistic origin. We suggest that a comparative analysis of mechanisms for pulsing in these and other systems will be a very fruitful way to uncover core conserved circuitry for pulse generation and to understand the ways in which this core circuitry is tuned or accessorized in different contexts to achieve different functional outcomes.

Materials and methods

C. elegans culture and strains

We cultured *C. elegans* strains at 22°C under standard conditions (Brenner, 1974). Table 1 lists the mutations and transgenes used in this study. Unless otherwise specified, strains were provided by the Caenorhabditis Genetics Center, which is funded by the National Institutes of Health National Center for Research Resources.

RNAi

RNAi was performed by the feeding method as previously described (Timmons et al., 2001). Bacteria targeting *nmy-2*, *spd-5*, *rho-1*, *perm-1*, *arx-2*, *ani-1*, and *mlc-4* were obtained from the Kamath feeding library (Kamath et al., 2003). The L4417 plasmid targeting the entire GFP sequence (generated by the Fire laboratory and available at Rauzi et al. [2010], Levayer and Lecuit [2013], and He et al. [2010]) was transformed into HT115(DE3) bacteria. For the Myosin depletion experiments, L4 larvae coexpressing

Table 1. **List of strains used in this study**

Strain name	Genotype	Source
JJ1473	*unc-119(ed3)III; zuIs45 [nmy-2::NMY-2::GFP; unc-119(+)] V*	Nance et al., 2003
JH1541	*unc-119(ed3)III; pJH7.03 [unc-119(+); pie-1:GFP::ACT-5::pie-1 3′ UTR]*	Robin et al., 2014
EM198	*unc-119(ed3)III; mgSi5[cb-unc-119 (+) pie-1::GFP::ANI-1(AH+PH)]II; unc119(ed3)III; zuIs151 [nmy-2::NMY-2-mRFP; unc-119(+)] LG*	This study
EM45	*unc-119(ed3)III; ltIs28 [pASM14; pie-1::GFP-TEV-STAG::ANI-1::pie-1 3′ UTR; unc-119(+)]; zuIs151 [nmy-2::NMY-2::mRFP; unc-119(+)] LG*	This study
EM101	*unc-119(ed3)III; mgSi3[cb-unc-119(+) pie-1::GFP::utrophin::pie-1 3′ UTR] II; zuIs151 [nmy-2::NMY-2::mRFP; unc-119(+)] LG*	This study
EM85	*unc-119(ed3)III; zuIs45 [nmy-2::NMY-2::GFP; unc-119(+)]; zuIs151 [nmy-2::NMY-2::mRFP, unc-119(+)] LG*	This study
EM264	*unc-119(ed3)III; mgSi5[cb-unc-119 (+); pie-1::GFP::ANI-1(AH+PH)]II; nmy-2(cp52[nmy-2::mkate2 + LoxP unc-119(+) LoxP]) I*	This study
EM302	*mgSi5[cb-unc-119 (+) pie-1::GFP::ANI-1(AH+PH)]II; nmy-2(cp52[nmy-2::mkate2 + LoxP unc-119(+) LoxP]) I; rga-4(ok1935) unc-62(e644) rga-3(ok1988) V / nT1[qIs51] (IV;V)*	This study
EM301	*unc-119(ed3)III; nmy-2(cp52[nmy-2::mkate2 + LoxP unc-119(+) LoxP]) I; tSi25 [pOD928/EZ-36; prga-3::GFP::RGA-3; cb-unc-119(+)] II*	This study
EM291	[*unc-119(+) pie1::mCherry:Lifeact)*]; *tSi25 [pOD928/EZ-36; prga-3::GFP::RGA-3; cb-unc-119(+)]*	This study
EM200	*unc-119(ed3)III; unc-59(e261)I*; *mgSi5[cb-UNC-119 (+) pie-1::GFP::ANI-1(AH+PH)]II; zuIs151 [nmy-2::NMY-2-mRFP, unc-119(+)] LG*	This study

GFP::AHPH and NMY-2::mKate2 were transferred to *nmy-2* RNAi feeding plates 24–30 h before imaging. Strong depletion of myosin was verified by strong loss of cortical NMY-2::mKate2. For the ANI-1 depletion experiments, L4 larvae coexpressing GFP::AHPH and NMY-2::RFP, were transferred to *ani-1* RNAi feeding plates 30–36 h before imaging. For experiments involving *spd-5* RNAi, L4 larvae were transferred to feeding plates for 24–30 h before imaging. For the RhoA depletion experiments, synchronized young adults were transferred to *rho-1* RNAi plates 8–16 h before imaging. For experiments involving *mlc-4* RNAi, synchronized young adults were transferred to feeding plates for 12–16 h before imaging. For the LatA experiments, late L4 larvae were transferred to *perm-1* RNAi plates 16–24 h before imaging. For experiments involving *arx-2* RNAi, L4 larvae were transferred to feeding plates for 30–36 h before imaging.

Microscopy

We mounted embryos as described previously (Robin et al., 2014) on glass slides under #1.5 coverslips in 3–5 µl of standard Egg Salts containing ~100 uniformly sized polystyrene beads (18.7 ± 0.03 µm diameter; no. NT29N; Bangs Laboratories). The beads acted as spacers and allowed us to achieve uniform compression of the embryo surface across experiments (Robin et al., 2014).

We performed all imaging at 21–23°C on a Nikon ECLIPSE-Ti inverted microscope equipped with a Ti-ND6-PFS Perfect Focus Unit. A laser merge module (Spectral Applied Research) controlled fast, tunable delivery of 481-nm and 561-nm laser excitation from 50 mW solid-state lasers (Coherent Technology) to a motorized TIRF illuminator. We adjusted the laser illumination angle to achieve near-TIRF illumination (Tokunaga et al., 2008). We collected images using a Nikon CFI Apo 1.45 NA oil immersion TIRF objective combined with 1.5× intermediate magnification onto an Andor iXon3 897 EMCCD camera. All image acquisition was controlled by using Metamorph software. We used ImageJ to set minimum and maximum pixel values and perform gamma adjustments on the original 16-bit image data before converting images to 8-bit red, green, blue format or grayscale format for display. We performed these operations identically for all images that are compared directly.

Single-molecule imaging

We performed single-molecule imaging as described previously (Robin et al., 2014). For NMY-2::GFP, we used a combination of RNAi against GFP and mild photobleaching in wide-field-illumination mode to reduce surface densities of GFP-tagged transgenic proteins to single-molecule levels. For GFP::Actin, which is expressed at very low levels in the strain that we used, we used mild photobleaching alone. For GFP::Actin and NMY-2::GFP, we imaged single molecules using 10% laser power (~0.16 µW/µm^2), with 100-ms exposures in continuous streaming mode (GFP::Actin and NMY-2::GFP), yielding an approximate photobleaching rate of 0.05/s (Robin et al., 2014).

Analysis of F-actin and Myosin II turnover

In previous work, we compared two methods for estimating local F-actin disassembly rates from single-molecule data (Robin et al., 2014). The first method (smPReSS) estimates average disassembly rates in a local region by fitting kinetic models to the approximately exponential decay in particle densities measured during photobleaching, assuming steady-state conditions. The second method relies on single-molecule detection and tracking and infers appearance and disappearance events directly from single-molecule trajectories. We showed that, under steady-state conditions and when Myosin II is inhibited to remove the effects of local contraction and cortical flow, these two methods yield estimates of local disassembly that agree to within 20%. During pulsed contractions, the steady-state assumption is not valid, and the effects of cortical flow cannot be ignored. Therefore, in this work, we relied exclusively on the particle-tracking method to measure local appearance, disappearance, and motion of single molecules.

In preliminary analyses, we found that single molecules of GFP::Actin and NMY-2::GFP move sufficiently slowly during pulsed contractions that we could obtain marginally better results by pre-averaging 10 consecutive frames of raw data to produce sequences of images at 1-s intervals. We performed single-molecule detection and tracking on this pre-averaged data using a MATLAB implementation of the Crocker-Grier method (Crocker, 1996; Pelletier et al., 2009). We then inferred single-molecule appearance and disappearance events and frame-to-frame single-molecule displacements directly from the single-molecule trajectories.

Measuring local deformations from single-molecule data

The key goal of our single-molecule analysis was to distinguish the relative contributions of local assembly/disassembly and local deformation/flow to changes in local density during pulsed contractions. To do so, it was essential to follow dynamic changes in assembly/disassembly on a moving and contracting patch of cortex, i.e., in a material (Lagrangian) frame of reference. We used single-molecule displacements to identify and track regions of cortex undergoing pulsed contractions as follows.

Tracking a polygonal ROI during individual pulses

For each pulse, we identified a reference time point at/near the onset of contraction by visual inspection of the time-lapse sequence. At this time point, we identified manually an elliptical region containing the patch of cortex undergoing contraction (Fig. S1 A). We computed the smallest polygon (the "convex hull") containing all the particles detected within the elliptical region (Fig. S1 B). Each vertex of the reference polygon was thus associated with a single molecule detected on the cell surface. To propagate the polygonal ROI forward and backward in time, we computed the frame-to-frame displacement of each of its vertices, either from the displacement of a vertex-associated molecule or (once the molecule disappears) from a weighted average of the frame-to-frame displacements of nearby particles (Fig. S1 C). We then measured local deformation and turnover within this polygonal ROI as follows.

Measuring local deformation and turnover during individual pulses

We compared three different measures of local compression (or dilation) within the polygonal ROI from frame to frame (Fig. S2 A): the change in normalized surface area, a particle-based strain rate, and a material strain rate. We computed the change in surface area s_A as the time-derivative of the normalized area of the polygonal ROI:

$$s_A(t) \;=\; \frac{A_{t+1} - A_t}{\langle A \rangle},$$

where $\langle A \rangle$ is the mean surface area taken over all frames in the pulse sequence. To compute a particle-based strain rate, for each particle in the polygonal ROI, we computed the average normalized change in distance between that particle and its near-neighbors:

$$s_P^i(t) \;=\; \frac{1}{M}\left(\sum\nolimits_{j=1\ldots M}\frac{d_{ij}^{t+1} - d_{ij}^{t}}{d_{ij}^{t}}\right),$$

where d_{ij}^t is the distance between particle i and a near-neighbor particle j at time t, and the sum is taken over all neighbor particles within a disk of radius 20 pixels centered on particle i. We then averaged over all particles in the ROI to obtain a particle-based strain rate for the entire ROI:

$$s_P(t) \;=\; \frac{1}{N}\left(\sum\nolimits_{i=1\ldots N} s_P^i(t)\right).$$

Finally, to compute a material strain rate s_M, we used a linear least squares regression method to estimate the local gradient of particle velocities (Landau and Lifshitz, 1987). We then decomposed the resulting velocity gradient tensor into antisymmetric (rotation) and symmetric (strain rate) components. We then took one-half the trace of the symmetric strain-rate tensor as a measure of local compressive strain. In practice, we found that all three methods yielded very similar results regarding the magnitude and timing of contractions (Fig. S2 A). We report results based on the particle-based strain rate in Figs. 2 and 3.

Measuring turnover

To quantify turnover rates for F-actin or Myosin II within the polygonal ROI, for each time point t, we measured the area of the ROI (A_t), the number of particles N_t, their density $D_t = N_t/A_t$,and the number of appearance and disappearance events that occurred within the ROI between time t and $t + \Delta t(\Delta N_t^+, \Delta N_t^-)$. We quantified the mean appearance rate and the mean disappearance rates within the ROI as $k_t^+ \;=\; \Delta N_t^+/\Delta t$ and $k_t^- \;=\; \Delta N_t^-/N_t\Delta t$. We computed the change in actin density within a polygonal ROI at time t as $\Delta D_t \;=\; D_{t+\Delta t} - D_t$. We estimated the contribution to the change in density from deformation of the ROI to be $\Delta D_{deformation} \;=\; -D_t s_P$, where s_p is the particle-based strain rate measured as described above, and the contribution from turnover (i.e., net imbalance of appearance and disappearance) to be $\Delta D_{turnover} \;=\; (N_{t+\Delta t} - N_t)/A_{t+\Delta t}$, such that $\Delta D_t = \Delta D_{deformation} + \Delta D_{turnover}$.

Two-color imaging, pulse tracking, and analysis

We performed two-color imaging using the imaging system described above with near-TIRF illumination. We performed the initial steps of image processing, pulse identification and extraction, using the software package ImageJ (National Institutes of Health). For all subsequent steps, including pulse tracking, intensity measurements, data normalization, and alignment across multiple pulses, we used custom functions written in MATLAB (Mathworks).

We imaged embryos coexpressing GFP- and RFP-tagged transgenes by alternating 100-ms exposures with 488-nm and 561-nm excitation, thus giving five two-color frames per second. We used 25% maximum laser power ≈0.4 µW/µm² for each channel. For subsequent analysis, we averaged more than five consecutive frames to obtain a single image for each channel at 1-s intervals. We limited our analysis to individual pulses that moved very little during the period leading up to the onset of contraction. We used ImageJ to extract a subregion containing each pulse of interest. With the exception of Myosin-depleted embryos, we used NMY-2::RFP as a reference signal to track the location of the pulse through time. For the analysis of Myosin-depleted embryos, we used GFP::AHPH as the reference signal.

We used the reference signal to identify and track a moving ROI associated with each pulse as follows (Fig. S3 A). First, we smoothed each frame of the image sequence using a gaussian filter (sigma = 2–3 µm). We then thresholded the smoothed image to identify ROIs associated with the pulse in consecutive frames. We used the same value of sigma and the same threshold for all frames, and we chose these values such that each ROI in the sequence was simply connected and such that the largest ROI in the sequence was approximately the same size as the region of strong signal accumulation near the peak of the pulse in the unprocessed data, as viewed by eye.

To measure signal intensities versus time during a pulse, we first used MATLAB to determine the centroid of each of the ROIs identified above to obtain a sequence of centroid positions $C_t = (x_t, y_t)$. We extended this sequence backward in time using the first measured centroid position C_{first} and extended it forward in time using the last measured centroid position C_{last}. We then used a single reference ROI, centered on positions $\left[C_{first-N},\ldots,C_{last+N}\right]$, to measure a sequence of GFP and RFP intensities over time. We compared two different reference ROIs: (a) the largest ROI measured in the sequence, which corresponds roughly to peak accumulation of Myosin II and (b) a "bounding box," defined to be the smallest square region containing this largest ROI. Because the results did not differ significantly, we used the bounding box ROI for all measurements reported here.

For each probe, we measured the mean signal intensity in the entire ROI over time. We then normalized these data for individual pulses using the equation

$$I_{norm}(t) = \frac{I_{mean}(t) - I_{\min}}{I_{\max} - I_{\min}},$$

where $I_{mean}(t)$ is the mean intensity in the ROI at time t, I_{min} is the minimum mean intensity in the ROI before the onset of contraction, I_{max} is the maximum mean intensity in the ROI measured over the entire sequence $\left[C_{first-N},\ldots,C_{last+N}\right]$. Finally, we aligned data across multiple pulses with respect to the time point at which NMY-2::RFP crossed 25% of its normalized maximum intensity (Fig. S3 C). The mean was calculated with a 95% confidence interval.

To partition the AHPH::GFP signal into diffuse and myosin colocalized fractions, we defined a myosin colocalized mask to be the collection of pixels within the ROI in which the raw NMY-2::RFP signal was greater than a threshold percentage (75–95%) of its peak intensity, and the diffuse mask to be its complement (Fig. S3 D, top). We used these masks to decompose the total GFP::AHPH signal into diffuse and myosin-colocalized pools (Fig. S3 D, bottom). We then partitioned the total normalized intensity within the ROI into diffuse and myosin-colocalized signals given by

$$S_D(t) \;=\; F_D \frac{I_D(t) - I_{\min}}{I_{\max} - I_{\min}}$$

and

$$S_C(t) \;=\; F_C(t) \frac{I_C(t) - I_{\min}}{I_{\max} - I_{\min}},$$

where $F_D(t)$ and $F_C(t)$ are the fraction of pixels, and $I_D(t)$ and $I_C(t)$ are the mean intensities, in the diffuse and myosin-colocalized regions respectively (Fig. S3, E and F). The timing with which the diffuse and myosin-colocalized signals rose and fell was insensitive to the exact threshold. We used 95% for the results reported here.

We performed several additional controls to assess the sensitivity of our results to variation across strains, or the details of pulse identification, tracking and intensity measurements. First, we compared the kinetics of Myosin II accumulation during pulses in embryos coexpressing NMY-2::GFP and NMY-2::RFP and confirmed that the dynamics of accumulation were essentially identical after normalizing for differences in expression level and probe brightness (Fig. 4, E and F; and Fig. S3, G and H). Second, we confirmed that the dynamics of Myosin::RFP accumulation was essentially identical across the different two-color strains that we used (Fig. S3, G and H). Finally, we verified that our measurements of the rate and relative timing of accumulation of different signals were largely insensitive to differences in the size of the box/blobs used (Fig. S3 and data not shown).

Kymograph analysis

To produce the kymographs shown in Figs. 5, 6, 7, 8, 9, and S4, we aligned images so that the anterior–posterior axis of the embryo coincided with the horizontal (x) image axis. We selected rectangular regions aligned with the x image axis, whose width (in x) coincided with the embryonic ROI and whose height (in y) was 10–20 pixels. From the original image stack, we extracted an xyt substack corresponding to this rectangular region; we used ImageJ's reslice tool to reslice this stack with respect to the xt plane, and then we used a maximum-intensity projection to collapse the individual slices in y to obtain a kymograph in x versus t. For the kymographs in Fig. 4 C and S4 C, we selected the indicated regions aligned with the vertical (y) axis and resliced with respect to the yt plane.

Colocalization analysis

We analyzed colocalization of mCherry::Lifeact and GFP::RGA-3 signals using the ImageJ plugin Coloc_2 (https://imagej.net/Coloc_2). Given a pair of image stacks representing the two signals for a sequence of frames within a ROI, we first scaled the data for each stack to lie between 0 and 255, then used Coloc_2 to compute Pearson's correlation coefficient and an associated significance value and to estimate Mander's correlation coefficients with automated threshold determination (Costes et al., 2004).

Statistical analysis methods

We computed 95% confidence intervals for pulse intensity data assuming a normal distribution. We tested differences between samples using a two-tailed *t* test, assuming normal distributions with unequal variances.

Modeling RhoA pulse generation

We built a simple ordinary differential equation model for RhoA pulse generation at a single point in space based on autocatalytic activation of RhoA and delayed negative feedback via RhoA-dependent recruitment of RGA-3/4. We started with the following assumptions:

(1) RhoA is activated at a constant basal rate.

(2) Active RhoA feeds back to promote further RhoA activation at a rate that can be described as a Hill function of RhoA density.

(3) RGA-3 and RGA-4 can be treated as a single species (RGA-3/4) that acts as a GAP to promote local inactivation of RhoA.

(4) Active RhoA promotes local F-actin assembly; RGA-3/4 binds F-actin from an abundant cytoplasmic pool, and dissociates from F-actin at a constant rate. Because RGA-3 and F-actin accumulate with very similar kinetics, we did not model F-actin directly. Instead, we assumed that RGA-3/4 binds the cortex at a constant basal rate plus a rate that depends on the local density of active RhoA and that RGA-3/4 dissociates from the cortex at a constant rate.

(5) To capture the observed delay between the sharp upswing in RhoA activity and the onset of F-actin and RGA-3/4 accumulation (Fig. 4 D and Fig. 7 B), we assumed ultrasensitive dependence of RGA-3/4 recruitment rate on RhoA activity.

With these assumptions, letting ρ represent the density of RhoA and r represent the density of RGA-3/4, we write a pair of ordinary differential equations for ρ and r:

$$\begin{aligned}\frac{d\rho}{dt} &= k_\rho^0 + k_\rho^{fb}\frac{\rho^n}{K_{fb}+\rho^n} - k_{GAP}\, r\frac{\rho}{K_{GAP}+\rho}\\ \frac{dr}{dt} &= k_r^0 + k_r^{ass}\rho^m - k_r^{diss} r.\end{aligned}$$

Estimating model parameter values

We estimated the values for model parameters; we first constructed empirical relationships between intensities of GFP::AHPH and GFP::RGA-3 (hereafter RhoA and RGA) and their time derivatives during pulses of RhoA activity. Intensity data for RhoA and RGA were normalized, aligned, and averaged over many individual pulses, then coaligned using Myosin::RFP as a common reference as described above (Fig. 7 C). We smoothed these data using a five-frame moving average and then estimated the time derivatives of signal intensity as the difference in intensities between consecutive frames. We then fit model equations to these data as follows: First, we fixed reference values for basal RhoA activation ($k_\rho^0 = 0.001$) and RGA recruitment ($k_r^0 = 0.001$), consistent with the slow rates of increase in RhoA and RGA observed before the sharp upswing of each pulse (Fig. 7 A). To estimate parameters that govern RhoA dynamics, we first considered the rising phase of RhoA activation (colored segments of the curves in Fig. 10 B), when RGA is ~0, and used nonlinear least squares regression to fit

$$k_\rho^0 + k_\rho^{fb}\frac{\rho^n}{K_{fb}+\rho^n}$$

to data for dRhoA/dt versus RhoA (Fig. 10 C). We set $n = 1$, based on the observed form of dependence of dRhoA/dt on RhoA (Fig. 10 C), fixed the value of k_ρ^0, and used model fits to estimate values for k_ρ^{fb} and k_ρ^{fb}. Next, holding values for k_ρ^0, k_ρ^{fb}, and K_{fb} fixed, we fit the full equation for dp/dt to data for dRhoA/dt versus RhoA and RGA for the termination phase (colored segments of the curves in Fig. 10 D) to estimate values for k_{GAP} and K_{GAP} (Fig. 10 E). These fits yielded a value for K_{GAP} that was consistently negative and close to zero, corresponding to a scenario in which RGA-3/4 operates near saturation on active RhoA. Therefore, in subsequent analyses, we set K_{GAP} to a small constant positive value ($K_{GAP} = 0.001$) and used the model fit to estimate a value for k_{GAP}. To estimate parameters that govern RhoA dynamics, we fit the full equation for dr/dt to data for dRGA/dt versus RhoA and RGA over the entire pulse (Fig. 10 G).

For each set of parameters determined as above, we set the initial values for r and p to zero, simulating a scenario in which RhoA is minimally active and a small perturbation reduces RGA-3/4 to a minimally observed level. We then solved the equations numerically using MATLAB to determine if this initial perturbation would result in either a single pulse of RhoA activity followed by a return to a stable inactive state (excitability) or a train of pulses (oscillatory dynamics).

Online supplemental material

Fig. S1 shows the schematic overview of methods for tracking a moving and deforming patch of cortex from single molecule data. Fig. S2 shows the comparison of different methods to quantify local deformation (strain rate) and to align data across multiple pulses. Fig. S3 shows the measurement, alignment, and decomposition of fluorescence intensity data during pulsed contractions. Fig. S4 shows the two-color analysis of pulsed contractions in P0. Fig. S5 shows Septin localization and contributions to pulsed contractions in one-cell embryos. Video 1 shows the actomyosin pulse dynamics in wild-type cells expressing GFP::UTR and NMY-2::RFP. Video 2 shows a two-cell embryo expressing GFP::ACT-1 at single-molecule levels and imaged in near-TIRF mode. Video 3 shows dynamic tracking of a cortical patch from single-molecule data. Video 4 shows a two-cell embryo expressing NMY-2::GFP at single-molecule levels and imaged in near-TIRF mode. Video 5 shows the pulse dynamics in a two-cell embryo expressing GFP::AHPH and NMY-2::RFP. Video 6 shows the pulse dynamics in a P0 expressing GFP::AHPH and NMY-2::mKate and subjected to strong *nmy-2* RNAi. Video 7 shows the pulse dynamics in zygotes expressing GFP::AHPH and subjected to *rho-1 RNAi* for different periods of time. Video 8 shows the dynamics of GFP::RGA-3 and NMY-2::RFP accumulation during pulsing in AB cells. Video 9 shows the absence of RhoA pulsing in *rga-3; rga-4* double mutants. Video 10 shows the coordinated response of cortical F-actin and RGA-3 to acute treatment with LatA.

Acknowledgments

We thank Amy Maddox, Katrina Longhini, Dan Dickinson, Esther Zanin, and Karen Oegema for worm strains; Michael Glotzer, Margaret Gardel, Chip Ferguson, and members of the Munro laboratory for valuable discussions; and Katrina Longini for technical assistance.

This work was supported by National Institute of General Medical Sciences grants GM09844 (to E.M. Munro) and T32GM007197 (to J.B. Michaux). The content is solely the responsibility of the authors and does not necessarily represent the official views of the National Institutes of Health.

The authors declare no competing financial interests.

Author contributions**:** E.M. Munro conceived the project. J.B. Michaux and F.B. Robin shared equally in its intellectual development. F.B. Robin developed and applied the single molecule imaging and particle tracking analysis and performed all the work reported in Fig. 2 and 3. J.B. Michaux developed the multicolor imaging approach to analysis of pulsed contractions and performed the experiments reported in Fig. 4, 5, 6, 7, 8, and 9. W.M. McFadden and E.M. Munro performed the modeling shown in Fig. 10. J.B. Michaux, F.B. Robin, and E.M. Munro prepared figures and wrote the paper.

Submitted: 5 July 2018
Revised: 30 August 2018
Accepted: 5 September 2018

References

Allard, J., and A. Mogilner. 2013. Traveling waves in actin dynamics and cell motility. *Curr. Opin. Cell Biol.* 25:107–115. https://doi.org/10.1016/j.ceb.2012.08.012

Bement, W.M., M. Leda, A.M. Moe, A.M. Kita, M.E. Larson, A.E. Golding, C. Pfeuti, K.-C. Su, A.L. Miller, A.B. Goryachev, and G. von Dassow. 2015. Activator-inhibitor coupling between Rho signalling and actin assembly makes the cell cortex an excitable medium. *Nat. Cell Biol.* 17:1471–1483. https://doi.org/10.1038/ncb3251

Blanchard, G.B., S. Murugesu, R.J. Adams, A. Martinez-Arias, and N. Gorfinkiel. 2010. Cytoskeletal dynamics and supracellular organisation of cell shape fluctuations during dorsal closure. *Development.* 137:2743–2752. https://doi.org/10.1242/dev.045872

Bois, J.S., F. Jülicher, and S.W. Grill. 2011. Pattern formation in active fluids. *Phys. Rev. Lett.* 106:028103. https://doi.org/10.1103/PhysRevLett.106.028103

Bornens, M., M. Paintrand, and C. Celati. 1989. The cortical microfilament system of lymphoblasts displays a periodic oscillatory activity in the absence of microtubules: implications for cell polarity. *J. Cell Biol.* 109:1071–1083. https://doi.org/10.1083/jcb.109.3.1071

Brenner, S. 1974. The genetics of Caenorhabditis elegans. *Genetics.* 77:71–94.

Burkel, B.M., G. von Dassow, and W.M. Bement. 2007. Versatile fluorescent probes for actin filaments based on the actin-binding domain of utrophin. *Cell Motil. Cytoskeleton.* 64:822–832. https://doi.org/10.1002/cm.20226

Carvalho, A., S.K. Olson, E. Gutierrez, K. Zhang, L.B. Noble, E. Zanin, A. Desai, A. Groisman, and K. Oegema. 2011. Acute drug treatment in the early C. elegans embryo. *PLoS One.* 6:e24656. https://doi.org/10.1371/journal.pone.0024656

Chen, Q., S. Nag, and T.D. Pollard. 2012. Formins filter modified actin subunits during processive elongation. *J. Struct. Biol.* 177:32–39. https://doi.org/10.1016/j.jsb.2011.10.005

Costes, S.V., D. Daelemans, E.H. Cho, Z. Dobbin, G. Pavlakis, and S. Lockett. 2004. Automatic and quantitative measurement of protein-protein colocalization in live cells. *Biophys. J.* 86:3993–4003. https://doi.org/10.1529/biophysj.103.038422

Crocker, J. 1996. Methods of Digital Video Microscopy for Colloidal Studies. *J. Colloid Interface Sci.* 179:298–310. https://doi.org/10.1006/jcis.1996.0217

David, D.J.V., A. Tishkina, and T.J.C. Harris. 2010. The PAR complex regulates pulsed actomyosin contractions during amnioserosa apical constriction in Drosophila. *Development.* 137:1645–1655. https://doi.org/10.1242/dev.044107

De La Cruz, E.M., and M.L. Gardel. 2015. Actin mechanics and fragmentation. *J. Biol. Chem.* 290:17137–17144. https://doi.org/10.1074/jbc.R115.636472

Dierkes, K., A. Sumi, J. Solon, and G. Salbreux. 2014. Spontaneous oscillations of elastic contractile materials with turnover. *Phys. Rev. Lett.* 113:148102. https://doi.org/10.1103/PhysRevLett.113.148102

Diogon, M., F. Wissler, S. Quintin, Y. Nagamatsu, S. Sookhareea, F. Landmann, H. Hutter, N. Vitale, and M. Labouesse. 2007. The RhoGAP RGA-2 and LET-502/ROCK achieve a balance of actomyosin-dependent forces in C. elegans epidermis to control morphogenesis. *Development.* 134:2469–2479. https://doi.org/10.1242/dev.005074

Effler, J.C., Y.-S. Kee, J.M. Berk, M.N. Tran, P.A. Iglesias, and D.N. Robinson. 2006. Mitosis-specific mechanosensing and contractile-protein redistribution control cell shape. *Curr. Biol.* 16:1962–1967. https://doi.org/10.1016/j.cub.2006.08.027

Fernandez-Gonzalez, R., S.M. Simoes, J.C. Röper, S. Eaton, and J.A. Zallen. 2009. Myosin II dynamics are regulated by tension in intercalating cells. *Dev. Cell.* 17:736–743. https://doi.org/10.1016/j.devcel.2009.09.003

Goldbeter, A. 1996. Biochemical Oscillations and Cellular Rhythms: The Molecular Bases of Periodic and Chaotic Behavior. Cambridge University Press, Cambridge, UK. https://doi.org/10.1017/CBO9780511608193

Gorfinkiel, N. 2016. From actomyosin oscillations to tissue-level deformations. *Dev. Dyn.* 245:268–275. https://doi.org/10.1002/dvdy.24363

Graessl, M., J. Koch, A. Calderon, D. Kamps, S. Banerjee, T. Mazel, N. Schulze, J.K. Jungkurth, R. Patwardhan, D. Solouk, et al. 2017. An excitable Rho GTPase signaling network generates dynamic subcellular contraction patterns. *J. Cell Biol.* 216:4271–4285. https://doi.org/10.1083/jcb.201706052

Hamill, D.R., A.F. Severson, J.C. Carter, and B. Bowerman. 2002. Centrosome maturation and mitotic spindle assembly in C. elegans require SPD-5, a protein with multiple coiled-coil domains. *Dev. Cell.* 3:673–684. https://doi.org/10.1016/S1534-5807(02)00327-1

Hayakawa, K., H. Tatsumi, and M. Sokabe. 2011. Actin filaments function as a tension sensor by tension-dependent binding of cofilin to the filament. *J. Cell Biol.* 195:721–727. https://doi.org/10.1083/jcb.201102039

He, L., X. Wang, H.L. Tang, and D.J. Montell. 2010. Tissue elongation requires oscillating contractions of a basal actomyosin network. *Nat. Cell Biol.* 12:1133–1142. https://doi.org/10.1038/ncb2124

Hickson, G.R.X., and P.H. O'Farrell. 2008. Rho-dependent control of anillin behavior during cytokinesis. *J. Cell Biol.* 180:285–294. https://doi.org/10.1083/jcb.200709005

Izhikevich, E.M. 2007. Dynamical systems in neuroscience: The geometry of excitability and bursting. MIT Press, Cambridge, MA.

Jaffe, A.B., and A. Hall. 2005. Rho GTPases: biochemistry and biology. *Annu. Rev. Cell Dev. Biol.* 21:247–269. https://doi.org/10.1146/annurev.cellbio.21.020604.150721

Kamath, R.S., A.G. Fraser, Y. Dong, G. Poulin, R. Durbin, M. Gotta, A. Kanapin, N. Le Bot, S. Moreno, M. Sohrmann, et al. 2003. Systematic functional analysis of the Caenorhabditis elegans genome using RNAi. *Nature.* 421:231–237. https://doi.org/10.1038/nature01278

Kapustina, M., G.E. Weinreb, N. Costigliola, Z. Rajfur, K. Jacobson, and T.C. Elston. 2008. Mechanical and biochemical modeling of cortical oscillations in spreading cells. *Biophys. J.* 94:4605–4620. https://doi.org/10.1529/biophysj.107.121335

Kapustina, M., T.C. Elston, and K. Jacobson. 2013. Compression and dilation of the membrane-cortex layer generates rapid changes in cell shape. *J. Cell Biol.* 200:95–108. https://doi.org/10.1083/jcb.201204157

Kasza, K.E., and J.A. Zallen. 2011. Dynamics and regulation of contractile actin-myosin networks in morphogenesis. *Curr. Opin. Cell Biol.* 23:30–38. https://doi.org/10.1016/j.ceb.2010.10.014

Kim, H.Y., and L.A. Davidson. 2011. Punctuated actin contractions during convergent extension and their permissive regulation by the non-canonical Wnt-signaling pathway. *J. Cell Sci.* 124:635–646. https://doi.org/10.1242/jcs.067579

Koride, S., L. He, L.-P. Xiong, G. Lan, D.J. Montell, and S.X. Sun. 2014. Mechanochemical regulation of oscillatory follicle cell dynamics in the developing Drosophila egg chamber. *Mol. Biol. Cell.* 25:3709–3716. https://doi.org/10.1091/mbc.e14-04-0875

Kumar, K.V., J.S. Bois, F. Jülicher, and S.W. Grill. 2014. Pulsatory Patterns in Active Fluids. *Phys. Rev. Lett.* 112:208101. https://doi.org/10.1103/PhysRevLett.112.208101

Landau, L.D., and E.M. Lifshitz. 1987. Fluid Mechanics: Course of Theoretical Physics. Second edition. Vol. 6. Butterworth-Heinemann, Oxford, UK.

Levayer, R., and T. Lecuit. 2012. Biomechanical regulation of contractility: spatial control and dynamics. *Trends Cell Biol.* 22:61–81. https://doi.org/10.1016/j.tcb.2011.10.001

Levayer, R., and T. Lecuit. 2013. Oscillation and polarity of E-cadherin asymmetries control actomyosin flow patterns during morphogenesis. *Dev. Cell.* 26:162–175. https://doi.org/10.1016/j.devcel.2013.06.020

Loria, A., K.M. Longhini, and M. Glotzer. 2012. The RhoGAP domain of CYK-4 has an essential role in RhoA activation. *Curr. Biol.* 22:213–219. https://doi.org/10.1016/j.cub.2011.12.019

Luo, C.H., and Y. Rudy. 1991. A model of the ventricular cardiac action potential. Depolarization, repolarization, and their interaction. *Circ. Res.* 68:1501–1526. https://doi.org/10.1161/01.RES.68.6.1501

Luo, T., K. Mohan, V. Srivastava, Y. Ren, P.A. Iglesias, and D.N. Robinson. 2012. Understanding the cooperative interaction between myosin II and actin cross-linkers mediated by actin filaments during mechanosensation. *Biophys. J.* 102:238–247. https://doi.org/10.1016/j.bpj.2011.12.020

Machado, P.F., G.B. Blanchard, J. Duque, and N. Gorfinkiel. 2014. Cytoskeletal turnover and Myosin contractility drive cell autonomous oscillations in a model of Drosophila Dorsal Closure. *Eur. Phys. J. Spec. Top.* 223:1391–1402. https://doi.org/10.1140/epjst/e2014-02197-7

Maddox, A.S., B. Habermann, A. Desai, and K. Oegema. 2005. Distinct roles for two C. elegans anillins in the gonad and early embryo. *Development.* 132:2837–2848. https://doi.org/10.1242/dev.01828

Maddox, A.S., L. Lewellyn, A. Desai, and K. Oegema. 2007. Anillin and the septins promote asymmetric ingression of the cytokinetic furrow. *Dev. Cell.* 12:827–835. https://doi.org/10.1016/j.devcel.2007.02.018

Martin, A.C., M. Kaschube, and E.F. Wieschaus. 2009. Pulsed contractions of an actin-myosin network drive apical constriction. *Nature.* 457:495–499. https://doi.org/10.1038/nature07522

Mason, F.M., S. Xie, C.G. Vasquez, M. Tworoger, and A.C. Martin. 2016. RhoA GTPase inhibition organizes contraction during epithelial morphogenesis. *J. Cell Biol.* 214:603–617. https://doi.org/10.1083/jcb.201603077

Motegi, F., and A. Sugimoto. 2006. Sequential functioning of the ECT-2 RhoGEF, RHO-1 and CDC-42 establishes cell polarity in Caenorhabditis elegans embryos. *Nat. Cell Biol.* 8:978–985. https://doi.org/10.1038/ncb1459

Munjal, A., J.-M. Philippe, E. Munro, and T. Lecuit. 2015. A self-organized biomechanical network drives shape changes during tissue morphogenesis. *Nature.* 524:351–355. https://doi.org/10.1038/nature14603

Munro, E., J. Nance, and J.R. Priess. 2004. Cortical flows powered by asymmetrical contraction transport PAR proteins to establish and maintain anterior-posterior polarity in the early C. elegans embryo. *Dev. Cell.* 7:413–424. https://doi.org/10.1016/j.devcel.2004.08.001

Naganathan, S.R., S. Fürthauer, M. Nishikawa, F. Jülicher, and S.W. Grill. 2014. Active torque generation by the actomyosin cell cortex drives left-right symmetry breaking. *eLife.* 3:e04165. https://doi.org/10.7554/eLife.04165

Nance, J., E.M. Munro, and J.R. Priess. 2003. C. elegans PAR-3 and PAR-6 are required for apicobasal asymmetries associated with cell adhesion and gastrulation. *Development*. 130:5339–5350. https://doi.org/10.1242/dev.00735

Nishikawa, M., S.R. Naganathan, F. Jülicher, and S.W. Grill. 2017. Controlling contractile instabilities in the actomyosin cortex. *eLife.* 6:e19595. https://doi.org/10.7554/eLife.19595

Olson, S.K., G. Greenan, A. Desai, T. Müller-Reichert, and K. Oegema. 2012. Hierarchical assembly of the eggshell and permeability barrier in C. elegans. *J. Cell Biol.* 198:731–748. https://doi.org/10.1083/jcb.201206008

Paluch, E., M. Piel, J. Prost, M. Bornens, and C. Sykes. 2005. Cortical actomyosin breakage triggers shape oscillations in cells and cell fragments. *Biophys. J.* 89:724–733. https://doi.org/10.1529/biophysj.105.060590

Pelletier, V., N. Gal, P. Fournier, and M.L. Kilfoil. 2009. Microrheology of microtubule solutions and actin-microtubule composite networks. *Phys. Rev. Lett.* 102:188303. https://doi.org/10.1103/PhysRevLett.102.188303

Piekny, A.J., and M. Glotzer. 2008. Anillin is a scaffold protein that links RhoA, actin, and myosin during cytokinesis. *Curr. Biol.* 18:30–36. https://doi.org/10.1016/j.cub.2007.11.068

Piekny, A.J., and A.S. Maddox. 2010. The myriad roles of Anillin during cytokinesis. *Semin. Cell Dev. Biol.* 21:881–891. https://doi.org/10.1016/j.semcdb.2010.08.002

Piekny, A.J., and P.E. Mains. 2002. Rho-binding kinase (LET-502) and myosin phosphatase (MEL-11) regulate cytokinesis in the early Caenorhabditis elegans embryo. *J. Cell Sci.* 115:2271–2282.

Piekny, A.J., J.-L.F. Johnson, G.D. Cham, and P.E. Mains. 2003. The Caenorhabditis elegans nonmuscle myosin genes nmy-1 and nmy-2 function as redundant components of the let-502/Rho-binding kinase and mel-11/myosin phosphatase pathway during embryonic morphogenesis. *Development.* 130:5695–5704. https://doi.org/10.1242/dev.00807

Pohl, C., M. Tiongson, J.L. Moore, A. Santella, and Z. Bao. 2012. Actomyosin-based self-organization of cell internalization during C. elegans gastrulation. *BMC Biol.* 10:94. https://doi.org/10.1186/1741-7007-10-94

Rankin, K.E., and L. Wordeman. 2010. Long astral microtubules uncouple mitotic spindles from the cytokinetic furrow. *J. Cell Biol.* 190:35–43. https://doi.org/10.1083/jcb.201004017

Rauzi, M., P.-F. Lenne, and T. Lecuit. 2010. Planar polarized actomyosin contractile flows control epithelial junction remodelling. *Nature.* 468:1110–1114. https://doi.org/10.1038/nature09566

Razzell, W., W. Wood, and P. Martin. 2014. Recapitulation of morphogenetic cell shape changes enables wound re-epithelialisation. *Development.* 141:1814–1820. https://doi.org/10.1242/dev.107045

Ren, Y., J.C. Effler, M. Norstrom, T. Luo, R.A. Firtel, P.A. Iglesias, R.S. Rock, and D.N. Robinson. 2009. Mechanosensing through cooperative interactions between myosin II and the actin crosslinker cortexillin I. *Curr. Biol.* 19:1421–1428. https://doi.org/10.1016/j.cub.2009.07.018

Robin, F.B., W.M. McFadden, B. Yao, and E.M. Munro. 2014. Single-molecule analysis of cell surface dynamics in Caenorhabditis elegans embryos. *Nat. Methods.* 11:677–682. https://doi.org/10.1038/nmeth.2928

Salbreux, G., J.F. Joanny, J. Prost, and P. Pullarkat. 2007. Shape oscillations of non-adhering fibroblast cells. *Phys. Biol.* 4:268–284. https://doi.org/10.1088/1478-3975/4/4/004

Schiffhauer, E.S., T. Luo, K. Mohan, V. Srivastava, X. Qian, E.R. Griffis, P.A. Iglesias, and D.N. Robinson. 2016. Mechanoaccumulative Elements of the Mammalian Actin Cytoskeleton. *Curr. Biol.* 26:1473–1479. https://doi.org/10.1016/j.cub.2016.04.007

Schmutz, C., J. Stevens, and A. Spang. 2007. Functions of the novel RhoGAP proteins RGA-3 and RGA-4 in the germ line and in the early embryo of C. elegans. *Development.* 134:3495–3505. https://doi.org/10.1242/dev.000802

Schonegg, S., and A.A. Hyman. 2006. CDC-42 and RHO-1 coordinate acto-myosin contractility and PAR protein localization during polarity establishment in C. elegans embryos. *Development.* 133:3507–3516. https://doi.org/10.1242/dev.02527

Schonegg, S., A.T. Constantinescu, C. Hoege, and A.A. Hyman. 2007. The Rho GTPase-activating proteins RGA-3 and RGA-4 are required to set the initial size of PAR domains in Caenorhabditis elegans one-cell embryos. *Proc. Natl. Acad. Sci. USA.* 104:14976–14981. https://doi.org/10.1073/pnas.0706941104

Sedzinski, J., M. Biro, A. Oswald, J.-Y. Tinevez, G. Salbreux, and E. Paluch. 2011. Polar actomyosin contractility destabilizes the position of the cytokinetic furrow. *Nature.* 476:462–466. https://doi.org/10.1038/nature10286

Segal, D., A. Zaritsky, E.D. Schejter, and B.-Z. Shilo. 2018. Feedback inhibition of actin on Rho mediates content release from large secretory vesicles. *J. Cell Biol.* 217:1815–1826. https://doi.org/10.1083/jcb.201711006

Severson, A.F., D.L. Baillie, and B. Bowerman. 2002. A Formin Homology protein and a profilin are required for cytokinesis and Arp2/3-independent assembly of cortical microfilaments in C. elegans. *Curr. Biol.* 12:2066–2075. https://doi.org/10.1016/S0960-9822(02)01355-6

Solon, J., A. Kaya-Copur, J. Colombelli, and D. Brunner. 2009. Pulsed forces timed by a ratchet-like mechanism drive directed tissue movement during dorsal closure. *Cell.* 137:1331–1342. https://doi.org/10.1016/j.cell.2009.03.050

Strogatz, S. 1994. Nonlinear dynamics and chaos with applications to physics, biology, chemistry, and engineering. CRC Press, Boca Raton, FL.

Timmons, L., D.L. Court, and A. Fire. 2001. Ingestion of bacterially expressed dsRNAs can produce specific and potent genetic interference in Caenorhabditis elegans. *Gene.* 263:103–112. https://doi.org/10.1016/S0378-1119(00)00579-5

Tokunaga, M., N. Imamoto, and K. Sakata-Sogawa. 2008. Highly inclined thin illumination enables clear single-molecule imaging in cells. *Nat. Methods.* 5:159–161. https://doi.org/10.1038/nmeth1171

Tse, Y.C., A. Piekny, and M. Glotzer. 2011. Anillin promotes astral microtubule-directed cortical myosin polarization. *Mol. Biol. Cell.* 22:3165–3175. https://doi.org/10.1091/mbc.e11-05-0399

Tse, Y.C., M. Werner, K.M. Longhini, J.-C. Labbé, B. Goldstein, and M. Glotzer. 2012. RhoA activation during polarization and cytokinesis of the early Caenorhabditis elegans embryo is differentially dependent on NOP-1 and CYK-4. *Mol. Biol. Cell.* 23:4020–4031. https://doi.org/10.1091/mbc.e12-04-0268

Vallotton, P., S.L. Gupton, C.M. Waterman-Storer, and G. Danuser. 2004. Simultaneous mapping of filamentous actin flow and turnover in migrating cells by quantitative fluorescent speckle microscopy. *Proc. Natl. Acad. Sci. USA.* 101:9660–9665. https://doi.org/10.1073/pnas.0300552101

Vasquez, C.G., M. Tworoger, and A.C. Martin. 2014. Dynamic myosin phosphorylation regulates contractile pulses and tissue integrity during epithelial morphogenesis. *J. Cell Biol.* 206:435–450. https://doi.org/10.1083/jcb.201402004

Watanabe, N., and T.J. Mitchison. 2002. Single-molecule speckle analysis of actin filament turnover in lamellipodia. *Science.* 295:1083–1086. https://doi.org/10.1126/science.1067470

Weiner, O.D., W.A. Marganski, L.F. Wu, S.J. Altschuler, and M.W. Kirschner. 2007. An actin-based wave generator organizes cell motility. *PLoS Biol.* 5:e221. https://doi.org/10.1371/journal.pbio.0050221

Werner, M., E. Munro, and M. Glotzer. 2007. Astral signals spatially bias cortical myosin recruitment to break symmetry and promote cytokinesis. *Curr. Biol.* 17:1286–1297. https://doi.org/10.1016/j.cub.2007.06.070

White, J.G., and G.G. Borisy. 1983. On the mechanisms of cytokinesis in animal cells. *J. Theor. Biol.* 101:289–316. https://doi.org/10.1016/0022-5193(83)90342-9

Zanin, E., A. Desai, I. Poser, Y. Toyoda, C. Andree, C. Moebius, M. Bickle, B. Conradt, A. Piekny, and K. Oegema. 2013. A conserved RhoGAP limits M phase contractility and coordinates with microtubule asters to confine RhoA during cytokinesis. *Dev. Cell.* 26:496–510. https://doi.org/10.1016/j.devcel.2013.08.005

Zhang, D., and M. Glotzer. 2015. The RhoGAP activity of CYK-4/MgcRacGAP functions non-canonically by promoting RhoA activation during cytokinesis. *eLife.* 4:e08898. https://doi.org/10.7554/eLife.08898